STAR★METHODS

KEY RESOURCE TABLE

REAGENT or RESOURCE	SOURCE	IDENTIFIER
Experimental Models: Organisms/Strains		
D. melanogaster: Oregon-R, wild-type laboratory stock	N/A	Flybase: FBst1000077
D. melanogaster: chromosomal deletion spanning *hb* w[1118]; Df(3R)BSC477/TM6C, Sb[1] cu[1]	Bloomington *Drosophila* Stock Center	Flybase: FBab0045343 BDSC: 24981
Oligonucleotides		
smFISH probes for *hb*, see Table S1	This paper	N/A
smFISH probes for *Kr*, see Table S1	This paper	N/A
smFISH probes for *kni*, see Table S1	This paper	N/A
smFISH probes for *gt*, see Table S1	This paper	N/A
Software and Algorithms		
FiSH Toolbox	Little et al. (2013)	N/A

CONTACT FOR REAGENT AND RESOURCE SHARING

Further information and requests for resources and reagents should be directed to and will be fulfilled by the Lead Contact, Thomas Gregor (tg2@princeton.edu).

EXPERIMENTAL MODEL AND SUBJECT DETAILS

Fly strains

Oregon-R (Ore-R) embryos were used as wild-type. Embryos heterozygous for a deficiency spanning *hb* were collected from crosses of heterozygous adults of the strain w^{1118}; Df(3R)BSC477/TM6C. Heterozygotes of the *hb* deficiency, as well as wild-type male and female embryos stained for *gt*, were distinguished from siblings by visual inspection of nascent transcription sites.

METHOD DETAILS

DNA oligonucleotides

Oligonucleotide sequences complementary to the open reading frames of each gene of interest were chosen using the Biosearch Technologies Stellaris RNA FISH probe designer (https://www.biosearchtech.com/support/tools/design-software/stellaris-probe-designer). Amine-modified oligonucleotides were obtained from Biosearch Technologies, chemically coupled to NHS-ester-Atto565 (Sigma-Aldrich; 72464) or -Atto633 (Sigma-Aldrich; 01464) and purified by HPLC. Probes are listed in Table S1.

smFISH protocol

We modified our smFISH protocol (Little et al., 2013) to minimize background and maximize signal. Embryos were crosslinked in 1xPBS containing 16% paraformaldehyde for 2 min before devitellinization. Embryos were washed four times in methanol, 5 min per wash, with gentle rocking at room temperature, followed by an extended 30-60 min wash in methanol. Fixed embryos were then used immediately for smFISH without intervening storage. Embryos washed three times in 1X PBS, 5 min per wash, at room temperature with rocking. Embryos were then washed 3 times in smFISH wash buffer (Little et al., 2013), 10 min per wash, at room temperature. During this time, probes diluted in hybridization buffer (Little et al., 2013) were preheated to 37°C. Hybridization was performed for 1.5 hr at 37C with vigorous mixing every 15 min. During hybridization, smFISH wash buffer was preheated to 37C. Embryos were washed four times with large excess volumes of wash buffer for 3-5 min per wash, rinsed twice briefly in PBS, stained with DAPI, and mounted in VECTASHIELD (Vector Laboratories; H-1000). Imaging was performed within 48 hr to ensure high quality signal.

Imaging

Imaging was performed by laser-scanning confocal microscopy on a Leica SP5 inverted microscope. We used a 63x HCX PL APO CS 1.4 NA oil immersion objective with pixels of 76×76 nm^2 and z spacing of 340 nm. We typically obtained stacks representing 8μm in total axial thickness starting at the embryo surface. The microscope was equipped with "HyD Hybrid Detector" avalanche

photodiodes (APDs) that we utilized in photon counting mode. This is in contrast to our prior approach (Little et al., 2013) in which standard photomultiplier tubes (PMTs) were used to collect two separate smFISH image stacks at two different laser intensities: a low power stack for measuring transcription intensities, and a high power stack to distinguish single mRNAs. The use of low-noise photon-counting APDs in place of standard photomultipliers provided sufficient dynamic range to capture high signal transcription sites and to separate relatively dim cytoplasmic single mRNAs from background fluorescence with a single laser power. This also abrogated the need to calibrate the high- and low-power stacks for comparison. The removal of the calibration step provided an additional reduction in measurement error.

Image analysis

Raw data are processed according to previously developed image analysis pipeline (Little et al., 2013). Briefly, raw images are filtered using a Difference-of-Gaussians (DoG) filter to detect spot objects. A master threshold is applied to separate candidate spots from background. True point-like sources of fluorescence are identified, as they appeared on multiple consecutive z-slices (>3) at the same location. All candidate particles are then labeled as transcription sites, cytoplasmic transcripts or noise based on global thresholds. The threshold separating cytoplasmic transcripts from noise is defined as the bottom of the valley between the two peaks on the particle intensity distribution. The threshold for transcription sites depends both on intensity and position, as transcription sites cluster in z and are enclosed in nuclei (segmented from DAPI staining). Intensity of transcription sites is obtained by integrating the signal over a fixed cylinder volume ($V_s = \pi \times 0.76^2 \times 3.06\ \mu m^3$, determined from the objective's PSF).

Calibration in absolute units

We calibrated the integrated intensity of transcription sites F_s by first characterizing the relationship between the fluorescence signal and the density of cytoplasmic transcripts. We defined summation volumes in the embryo $(V \cong 3.8 \times 3.8 \times 8\ \mu m^3)$ avoiding region of high tissue deformation and excluding transcription site location. For each summation volume we counted the number of detected cytoplasmic transcripts and integrated the fluorescence intensity. At low count density, the fluorescence per summation volume F scales linearly with density D (Little et al., 2013). Fitting a simple linear relationship $F = \alpha D + \beta$, where β corresponds to background, enables estimation of a scaling factor α to calibrate transcription sites in "cytoplasmic units" (C.U.) for each embryo. Namely, the intensity in C.U. is given by $f = (F_s - bV_s)/\alpha$ where b is the background intensity per pixel in each nucleus. The resulting quantification of transcriptional activity for all gap genes is provided in Supplemental Data.

Measurement error

Embryo staging

In order to assess the timing of the different embryos, we first manually ranked the different embryos based on timing estimation from DAPI staining. We estimated the interphase stage relying on morphological features of the nuclei (shape and textures) in the DAPI channel. We then verified whether accumulation of cytoplasmic mRNAs correlates with our manual ranking (Figure S1A). Both approaches lead to similar results and provide a decent proxy for timing. By comparing the average activity of the different embryos in the maximally expressed regions with the cytoplasmic density, we assessed the effect of timing on the mean activity (Figure S1B). We estimated the Pearson correlation coefficient ρ for the different genes and regions (*gt* anterior and posterior regions). Overall, timing explain up to $\rho^2 = 44\%$ of the embryo variability (defined as the variance of the mean activity among embryos σ_μ^2) in the maximally expressed regions (Figure S1C), with the exception of *kni* that is highly correlated $\rho \sim 0.8$. We thus separated the *kni* embryos in two sub-populations, early and late embryos. We performed the splitting by finding the cytoplasmic density threshold that minimizes the sum of within-population variance in mean activity. We then calculated the staging variability $\sigma_{sta} = \rho\sigma_\mu$, defined as the variability in mean activity explained by timing between late and early embryos (Figure S1D). Given the overall small staging variability <14%, the total mean activity is stable enough to warrant the assumption of steady-state.

Imaging noise model

We quantified measurements noise due to imaging and calibration using a two-color smFISH approach, labeling each mRNA in alternating colors along the length of the mRNA. We included 15 *hb* embryos in the analysis, which corresponds to approximately 4,000 nuclei activity measurements. We then normalized the activity (fluorescence signal) of the nuclei in cytoplasmic units independently in each channel. In absence of noise and provided accurate normalization, both channels would perfectly correlate with slope one. By plotting one channel against the other (Figure 2A), we assessed the slope and characterized the spread of the data along the expected line.

We build a simple effective model to describe measurement noise:

$$P\left(S^{(5)}, S^{(3)} | G^{(5)}, G^{(3)}\right) = \mathcal{N}\left(S^{(5)} \mid \mu = G^{(5)}, \sigma_5^2\left(G^{(5)}\right)\right) \cdot \mathcal{N}\left(S^{(3)} \mid \mu = G^{(3)}, \sigma_3^2\left(G^{(3)}\right)\right) \quad \text{(Equation 1)}$$

where S stands for the fluorescent signal in cytoplasmic units and G the total nascent transcripts (in C.U.) in absence of noise. We assumed that the measurement errors were normally distributed and independent in both channels, which was motivated by the absence of correlation in the background. We further assumed that the variance would depend on activities, consistent with the

increasing spread observed in the data. In order to estimate the variance specific to each channel, we fitted a straight line $y = ax + h$ assuming error on both $x \equiv S^{(5)}$ and $y \equiv S^{(3)}$. We expanded the variance as a function of the scalar projection along the line v:

$$\sigma^2(v) = \sigma_b^2 + b_1 v + b_2 v^2 + \cdots$$

$$v = \frac{x + ay}{\sqrt{1 + a^2}}$$

Assuming the same error along x and y, we then maximized the following likelihood to estimate the parameters $\theta = \{a, h, \sigma_b, b_1, b_2, \cdots\}$:

$$P(\{x_i, y_i\} \mid \theta) = \prod_{i=1}^{N_d} \frac{1}{\sqrt{2\pi\sigma^2(v_i)}} \exp\left(-\frac{(y_i - ax_i - h)^2}{2(1 + a^2)\sigma^2(v_i)} \right)$$

Using the Akaike information criterion, we selected the best model which was parameterized by (a, σ_b, b_1, b_2) with $h = 0$. The best fitting parameters were: $a = 0.968$, $\sigma_b = 4.59 \cdot 10^{-2}$, $b_1 = 9.31 \cdot 10^{-3}$ and $b_2 = 9.23 \cdot 10^{-4}$ (Figure 2A). The variances in the noise measurement model (Equation 1) are then given by:

$$\sigma_5^2(G) = \sigma^2\left(v = \sqrt{G^2 + (aG)^2} \right)$$

$$\sigma_3^2(G) = \sigma^2\left(v = \sqrt{G^2 + (G/a)^2} \right)$$

where $\sigma^2(v) = \sigma_b^2 + b_1 v + b_2 v^2$. The resulting imaging noise is shown in Figure S1E. In the maximally expressed regions, we measure transcriptional activity with an error of 5% and relate it to absolute units with an uncertainty below 3.5% (the largest deviation of the slope 0.968 ± 0.003 from 1). This represents an error reduction by 3- to 4-fold compared to our previous measurements (assuming multiplicative errors; 6% versus 20%) (Little et al., 2013).

Splitting of the total variance

The Anterior-Posterior axis (AP) was determined based on a mid-sagittal elliptic mask of the embryo in the DAPI channel (Little et al., 2013). Position is obtained by registration of high- and low-magnification DAPI images of the surface. We then fitted constrained splines to approximate the mean activity as a function of the AP position. We used different features of the mean profiles such as maxima and inflection points to refine the alignment between the different embryos. Overall, this realignment procedure enables us to estimate an alignment error of the order of 2% egg length.

After alignment, we defined spatial bins along the AP-axis with a width of 2.5% of egg length. Such a width was a good compromise to balance the sampling and binning error. We next sought to decompose the measured total variance of the transcriptional activity σ^2 (Figure 1D) into different components related to imaging, alignment, embryo and nuclei variability (Figures 2B–2D). We first estimated the variability of the mean across embryos σ_μ^2 in each bin (Figure 2B); we split the total variance σ^2 in each bin according to the law of total variance:

$$\sigma^2 = \underbrace{\frac{1}{N_e}\sum_{i=1}^{N_e} \sigma_i^2}_{\sigma_i^2} + \underbrace{\frac{1}{N_e}\sum_{i=1}^{N_e} (\mu_i - \mu)^2}_{\sigma_\mu^2}$$

where N_e is the total number of embryos and μ the global mean.

Next we aimed to determine what fraction of σ_μ^2 is explained by residual misalignment. Assuming that all the variability in the mean at boundaries results from spatial misalignment of the different embryos, one can find an upper bound on the residual alignment error σ_x:

$$\sigma_\mu^2 \geq \sigma_{\text{ali}}^2 = \left(\frac{d\mu}{dx} \right)^2 \sigma_x^2$$

where μ is the global mean profile as function of AP position x. For each gene, we estimated the residual alignment error σ_x required to explain as much embryo variability as possible (Figure S1F, diagonal dash line). Overall we found that σ_x is of the order of 1% egg length. The total embryo variability in the maximally expressed regions cannot be explained by misalignment as $\left(\frac{d\mu}{dx} \right) \approx 0$ and leads to a noise floor (Figure S1F, horizontal dash line). This noise floor can be partly explained by variability in the stage (early versus late

interphase) of the different embryos (Figures S1C and S1D). In the following we thus split $\sigma^2_\mu = \sigma^2_{\text{ali}} + \sigma^2_{\text{emb}}$ where σ^2_{emb} is the residual embryo to embryo variability.

Finally, we assessed what fraction of the total variance σ^2 corresponds to combined measurement noise $\sigma^2_{\text{mea}} = \sigma^2_{\text{img}} + \sigma^2_{\text{ali}}$ where σ^2_{img} was estimated in subsection (STAR Methods, *Imaging noise model*). Total measurement noise σ^2_{mea} remains below 20% of the total variance for all genes and all position (Figure S1G), and on average reaches $6.1 \pm 3.5\%$. The remaining variability corresponds to biological variability $\sigma^2_{\text{bio}} = \sigma^2_{\text{nuc}} + \sigma^2_{\text{emb}}$ where σ^2_{nuc} is the nuclei variability and was defined as:

$$\sigma^2_{\text{nuc}} = \sigma^2 - \sigma^2_{\text{img}} - \sigma^2_{\text{ali}} - \sigma^2_{\text{emb}}$$

Overall, the non-nuclear variability $(\sigma^2_{\text{img}} + \sigma^2_{\text{ali}} + \sigma^2_{\text{emb}})$ remains below 33% of the total variance for all genes and all position (Figure S1H), and on average reaches $16.0 \pm 6.4\%$. Thus, the nuclei variability σ^2_{nuc} largely dominates in our data and represents 84% of the total variance on average (Figures 1E and 1F).

Single parameter distribution of transcriptional activity

Noise-mean relationship in the FISH data

In practice, we measure transcriptional activity in cytoplasmic units (intensity in equivalent number of fully elongated transcripts) and not in Pol II counts g directly. The measured mean activity μ in cytoplasmic units is proportional to the mean Pol II counts for a single gene copy $\langle g \rangle$, i.e., $\mu = C_1 N_g \langle g \rangle$ where $C_1 \in [0, 1]$ is a conversion factor accounting for the FISH probe locations on the gene and N_g the number of gene copies (for most gap genes $N_g = 4$, except for *gt* male and *hb* deficient that only have 2 copies). Assuming independence of loci, the measured variance σ^2follows a similar relationship, i.e., $\sigma^2 = C_2 N_g \sigma^2_g$ with $C_2 \in [0, 1]$. The conversion factors C_1 and C_2 are constants that are unique for each gene and are calculated further (STAR Methods, *Conversion factor for Pol II counts*).

As we will see later (Equation 8), one can derive the following functional form for the variance in Pol II counts for a single gene copy:

$$\sigma^2_g = \langle g \rangle + \langle g \rangle (g_0 - \langle g \rangle) \Phi$$

where g_0 is the maximal mean Pol II counts on the gene that is determined by the Pol II initiation rate k_{ini} and elongation time τ_e, and Φ a quantity that is related to the dynamics of the promoter activity and bounded $\Phi \in [0, 1]$. Of note, $\Phi = 0$ for a constitutively expressed gene such that the variance reduces to $\sigma^2_g = \langle g \rangle$ (Poisson variance). In principle, the values of both g_0 and Φ are gene-specific and could have specific dependency on $\langle g \rangle$. The interpretation of the equation above and the quantities g_0 and Φ will be discussed in greater details later on (STAR Methods, *Two-state model of transcriptional activity*). Using the relationships between the cytoplasmic units and Pol II counts for the mean and variance above, we can express the measured noise as:

$$\frac{\sigma^2}{\mu^2} = \frac{C_2}{C_1}\left(\frac{1}{\mu} + \frac{1}{C_1 N_g}\frac{\mu_0 - \mu}{\mu}\Phi\right)$$

where $\mu_0 = C_1 N_g g_0$ is the maximal mean expression level in cytoplasmic units. In practice, $C_2/C_1 \approx 1$ and $C_1 \approx 0.7$ (Table S2, 5′ probe location) such that the Poisson noise background in cytoplasmic units is approximately $1/\mu$. By setting $C_2/C_1 = 1$, we further simplify the equation above and obtain:

$$\frac{\sigma^2}{\mu^2} = \frac{1}{\mu}(1 + a(1 - \mu/\mu_0)) \qquad \text{(Equation 2)}$$

with $a = g_0 \Phi$. By assuming a and μ_0 constant, we found that the above noise-mean relationship (Equation 2) captures the overall trend in the data well (Figure 3A), with $a = 9.93 \pm 0.35$ and $\mu_0 = 53.07 \pm 1.73$ ($R^2 = 0.99$). Although both *gt* male and *hb* deficient follow a similar trend, they deviate from the black line, ($a = 10.66 \pm 0.35$, $\mu_0 = 18.52 \pm 0.28$) and ($a = 7.68 \pm 1.00$, $\mu_0 = 29.57 \pm 1.59$) respectively. Interestingly, despite the fact that g_0 and Φ could *a priori* be gene-specific, a is roughly conserved across genes and differences in μ_0 can be explained by variation in gene copies ($N_g = 2$ copies for *gt* male and *hb* deficient instead of 4) and gene length (*gt* is shorter than *hb*, Table S3). This suggests that some key quantities underlying transcription are conserved among the gap genes and can be highlighted by proper normalization of the measured activity.

Normalized cumulants for a single gene copy

To further investigate the transcriptional commonalities of the gap genes, we calculated the 2$^{\text{nd}}$, 3$^{\text{rd}}$ and 4$^{\text{th}}$ cumulants from the data (Figures 3B–3D). For independent random variables, the cumulants have the property to be extensive, which is convenient as the measured transcriptional activities result from the sum of 2 or 4 independent gene copies. We first converted the k^{th} cumulants $\tilde{\kappa}_k$ computed from the data in cytoplasmic units to Pol II counts (or number of nascent transcripts) for a single gene copy with a normalized gene length:

$$\kappa_k = \frac{1}{C_k N_g}\left(\frac{\langle L_g \rangle}{L_g}\right)^k \tilde{\kappa}_k$$

where κ_k is the k^{th} cumulant in Pol II counts for a single gene copy, L_g the gene length, N_g the gene copy number (4 for most genes, except *gt* male and *hb* deficient that only have 2 copies) and C_k a conversion factor for the k^{th} cumulant to ensure proper normalization of the Poisson background (Equation 3 and Table S2). The annotated gene length L_g varies between 1.8 to 3.6 kb for the gap genes. In the following we used an effective gene length that is slightly larger and takes into account the possible lingering of fully elongated transcripts at the loci (Table S3). This effective gene length can be estimated from the dual color FISH data (STAR Methods, *Dual color smFISH and effective gene length*). For the normalization, we used a normalized gene length of $\langle L_g \rangle = 3.3$ kb.

We then fitted a second order polynomial of the mean activity $\langle g \rangle$ to the variance σ_g^2 (Figures 3B and S2A) in order to estimate the maximal activity g_0, which was defined as the second crossing point between the Poisson background (Figure S2A dash line) and the fitted variance (solid line). We found $g_0 = 15.21 \pm 0.20$ Pol II for a normalized gene length of 3.3 kb. Similarly, we fitted 3rd and 4th order polynomial of the mean activity to the cumulants $\kappa_3$and κ_4 (Figures 3C and 3D), constrained to reach the Poisson limit at g_0. Of note, the cumulants of the Poisson distribution are all equal to the mean. As we observed in Figures 3B–3D, the polynomial fits (solid lines) capture the main trend observed in the data, suggesting a simple relationship between the cumulants and the mean. It follows that the underlying activity distribution is essentially a universal single parameter distribution whose parameter is the mean activity. To test the extent of the universality, we repeated the analysis above of each gap gene individually (Figures S2B–S2D). The individual fits (colored solid lines) remain relatively close to each other. Although the fits for *hb* slightly deviate from the other genes, the global shape of the cumulants is conserved.

Conversion factor for Pol II counts

As mentioned above, the cumulants of the transcriptional activity in cytoplasmic units are related to the cumulants in number of nascent transcripts or Pol II counts on the gene by conversion factors C_k. We calculated these conversion factors to ensure proper normalization of the Poisson background, meaning that the conversion of cumulants in C.U. for a constitutive gene would yield the correct cumulants in Pol II counts. Knowing the exact location of the fluorescent probe binding regions along the gene, one can calculate the contribution of a single nascent transcript to the signal in C.U. as a function its length l:

$$s(l) = \frac{1}{N}\sum_{i=1}^{N} H(l - l_i) = \frac{1}{N} b(l)$$

where H is the unit step function, l_i the end position of the i^{th} probe binding region and N the total number of probes. Here, we made the assumptions that each fluorescent probe contributes equally to the signal and each transcribed probe region bound. The number of probes bound to a transcript of length l is given by $b(l)$ and will be denoted b_i for $l \in (l_i, l_{i+1}]$ with $l_{N+1} = L_g$ the length of a fully elongated transcript. The total fluorescent signal s in cytoplasmic units for g transcripts is given by

$$s = \frac{1}{N}\sum_{i=1}^{N} b_i g_i$$

where $g = \sum_{i=1}^{N} g_i$, with g_i the number of transcripts whose length l belongs to the length interval $(l_i, l_{i+1}]$. Assuming that g_i follows a Poisson distribution with parameter $\lambda_i = k_{\text{ini}}\tau_i$ where $\tau_i = (l_{i+1} - l_i)/k_{\text{elo}}$, the mean fluorescent signal $\langle s \rangle$ is then given by

$$\langle s \rangle = \frac{1}{N}\sum_{i=1}^{N} b_i \langle g_i \rangle = \frac{1}{N}\sum_{i=1}^{N} b_i k_{\text{ini}}\tau_i = \underbrace{\left(\frac{1}{N}\sum_{i=1}^{N} b_i \tilde{\tau}_i\right)}_{C_1} k_{\text{ini}}\tau_e = C_1 \langle g \rangle$$

where $\tilde{\tau}_i = \tau_i/\tau_e = (l_{i+1} - l_i)/L$ and C_1 the conversion factor that relates the mean number of transcripts $\langle g \rangle$ to the mean fluorescent signal $\langle s \rangle$ in cytoplasmic units. This relation remains valid for the two-state model with $\langle g \rangle = k_{\text{ini}}\tau_e \langle n \rangle$ (Equation 7).

As for the mean, one can calculate the conversion factors for the higher moments and cumulants assuming a Poisson background. The second moment is given by

$$\langle s^2 \rangle = \frac{1}{N^2}\left\langle \sum_{ij} b_i b_j g_i g_j \right\rangle = \frac{1}{N^2}\left(\sum_{i \neq j} b_i b_j \langle g_i \rangle \langle g_j \rangle + \sum_i b_i^2 \langle g_i^2 \rangle\right)$$

$$= \frac{1}{N^2}\left(\sum_{i \neq j} b_i b_j k_{\text{ini}}^2 \tau_i \tau_j + \sum_i b_i^2 \left(k_{\text{ini}}^2 \tau_i^2 + k_{\text{ini}}\tau_i\right)\right)$$

$$= \frac{1}{N^2}\left(\sum_{ij} b_i b_j k_{\text{ini}}^2 \tau_i \tau_j + \sum_i b_i^2 k_{\text{ini}}\tau_i\right)$$

where $\langle g_i g_j \rangle = \langle g_i \rangle \langle g_j \rangle$ since initiation events are assumed independent. This only holds for the Poisson background and is no longer exact for the two-state model as the switching process would introduce correlations. Nevertheless, the conversion factors for the

higher moments and cumulants calculated below remain a good approximation under the two-state model, provided most probes are located in the 5′ region. The variance of the signal is finally given by

$$\left\langle (s-\langle s\rangle)^2 \right\rangle = \langle s^2\rangle - \langle s^2\rangle = \frac{1}{N^2}\sum_{i=1}^{N} b_i^2 k_{\text{ini}}\tau_i = \underbrace{\left(\frac{1}{N^2}\sum_{i=1}^{N} b_i^2\tilde{\tau}_i\right)}_{C_2}\langle g\rangle = C_2\langle g\rangle$$

The calculation above can be generalized to the 3rd and 4th cumulants. We found the following correction factor for the Poisson background:

$$C_k = \frac{1}{N^k}\sum_{i=1}^{N} b_i^k\tilde{\tau}_i \text{ for } k = 1,\cdots,4 \qquad \text{(Equation 3)}$$

Calculated values of C_k for each gene and two different configurations of probe locations (5′ or 3′ region) are given in Table S2.

Two-state model of transcriptional activity

Master equation

Transcriptional activity of a single gene copy was modeled as a telegraph process (on-off promoter switching) with transcript initiation occurring as a Poisson process during the 'on' periods (Peccoud and Ycart, 1995). Within the two-state model (Figure 3E), the distribution of nascent transcripts on a gene results from random Pol II initiation in the active state coupled with elongation and termination (Choubey et al., 2015; Senecal et al., 2014; Xu et al., 2016). For simplicity, we combined elongation and termination as an effective process that was modeled as a deterministic progression (constant Pol II elongation rate). In addition, we assumed that all the kinetic rates of the model are constant in time and identical across embryos. The kinetic parameters of the model are the initiation rate k_{ini}, the promoter switching rates k_{on} and k_{off}, and the elongation time $\tau_e = L_g/k_{\text{elo}}$.

The master equation that governs the temporal evolution of nascent transcripts at loci is given by

$$\frac{d}{dt}P_t(g,n) = k_{\text{ini}}\delta_{n1}(P_t(g-1,n) - P_t(g,n)) + k_n P_t(g,n-1) - k_{n+1}P_t(g,n) \qquad \text{(Equation 4)}$$

with g the number of nascent transcripts (or alternatively the number of Pol II) on the gene and n the promoter state. We used the convention that $n=1$ and $n=0$ correspond to the 'on' state and 'off' state respectively, and the following periodic conditions $n=-1\equiv 1$ and $n=2\equiv 0$. Here, δ stands for the Kronecker delta since initiation only occurs in the active state. Of note, we only considered the promoter switching and the initiation of elongation (Eq. 5); we did not explicitly model release of transcripts after termination. The rationale is the following; only the initiation events occurring during the time interval $[t-\tau_e, t]$ contributes to the signal at time t, i.e., the elongation time τ_e determined the 'memory' of the system. This is correct as long as the release events are instantaneous and termination is fast compared to elongation. Thus, the dynamics of nascent transcripts accumulation on the gene for $t \leq \tau_e$ is obtained by solving the master equation with zero initial transcript on the gene $P_{t_0}(g) = \delta_{g0}$ and an arbitrary initial distribution of promoter state.

Summary statistics

We can derive the temporal evolutions of the central moments from the master equation (Equation 4) (Lestas et al., 2008; Sánchez and Kondev, 2008). The means of nascent transcripts g and promoter states n satisfy the following equations:

$$\begin{cases} \dfrac{d}{dt}\langle g(t)\rangle = k_{\text{ini}}\langle n(t)\rangle \\ \dfrac{d}{dt}\langle n(t)\rangle = k_{\text{on}} - (k_{\text{on}}+k_{\text{off}})\langle n(t)\rangle \end{cases} \qquad \text{(Equation 5)}$$

At steady state $\left(\dfrac{d}{dt}\langle n\rangle = 0\right)$, the mean occupancy of the promoter is simply given by $\langle n\rangle = k_{\text{on}}/(k_{\text{on}}+k_{\text{off}})$. Similarly, the covariance satisfies the following set of equations:

$$\begin{cases} \dfrac{d}{dt}\sigma_g^2(t) = 2k_{\text{ini}}\sigma_{gn}(t) + k_{\text{ini}}\langle n(t)\rangle \\ \dfrac{d}{dt}\sigma_{gn}(t) = k_{\text{ini}}\sigma_n^2(t) - (k_{\text{on}}+k_{\text{off}})\sigma_{gn}(t) \\ \dfrac{d}{dt}\sigma_n^2(t) = -2(k_{\text{on}}+k_{\text{off}})\sigma_n^2(t) + k_{\text{on}}(1-\langle n(t)\rangle) + k_{\text{off}}\langle n(t)\rangle \end{cases} \qquad \text{(Equation 6)}$$

Assuming zero initial transcripts and promoter at steady state, one can solve both the mean and variance for g. Thus, the initial conditions are given by $\langle g(t_0)\rangle = 0$, $\langle n(t_0)\rangle = k_{\text{on}}/(k_{\text{on}}+k_{\text{off}})$, $\sigma_g^2(t_0) = 0$, $\sigma_{gn}(t_0) = 0$ and $\sigma_n^2(t_0) = \langle n(t_0)\rangle(1-\langle n(t_0)\rangle)$. Solving these equations (Equations 5 and 6) for the elongation time $t=\tau_e$ leads to:

$$\langle g\rangle = g_0\langle n\rangle \qquad \text{(Equation 7)}$$

$$\sigma_g^2 = g_0\langle n\rangle + g_0^2\langle n\rangle(1-\langle n\rangle)\Phi(\tau_e/\tau_n) \quad \text{(Equation 8)}$$

where $g_0 = k_{\text{ini}}\tau_e$ is the maximal mean nascent transcript number or equivalently the mean number of transcripts in a constitutive regime (gene always 'on') and $\Phi \in [0,1]$ a noise filtering function that takes into account the fluctuation correlation times. Here, the relevant timescales are the elongation time τ_e and the promoter switching correlation time $\tau_n = 1/(k_{\text{on}} + k_{\text{off}})$. The variance σ_g^2 results from the sum of two contributions; the Poisson variance $g_0\langle n\rangle$ stemming from the stochastic initiation of transcript and the propagation of switching noise:

$$\left(\frac{d\langle g\rangle}{d\langle n\rangle}\right)^2 \sigma_n^2 \Phi(\tau_e/\tau_n) = g_0^2 \underbrace{\langle n\rangle(1-\langle n\rangle)}_{\text{binomial variance}} \Phi(\tau_e/\tau_n)$$

For deterministic elongation, we find that the noise filtering function is given by:

$$\Phi(x) = 2\frac{\exp(-x)+x-1}{x^2}$$

In the limit of fast and slow promoter switching respectively, the noise filtering function reduces to

$$\tau_e \gg \tau_n \lim_{x\to\infty} \Phi(x) = 0$$

$$\tau_e \ll \tau_n \lim_{x\to 0} \Phi(x) = 1$$

Thus, the noise is minimal in the fast switching regime $\tau_e \gg \tau_n$ and reaches the Poisson limit $\sigma_g^2 = g_0\langle n\rangle$. While in the slow switching regime $\tau_e \ll \tau_n$, none of the switching noise is filtered and the variance is described by a second order polynomial of the mean occupancy $\langle n\rangle$, i.e., $\sigma_g^2 = g_0\langle n\rangle + g_0^2\langle n\rangle(1-\langle n\rangle)$. Of note, for exponentially distributed life-time of transcripts, such as cytoplasmic mRNA subject to degradation, the results above remain valid except that the noise averaging function becomes $\Phi(x) = 1/(1+x)$ with τ_e the average life-time of the transcripts.

Following a similar approach as in the previous paragraph, higher order moments and cumulants are analytically calculated from the master equations (Equation 4). The cumulants up to order 3 are equal to the central moments while higher order cumulants can be expressed as a combination of central moments. The 4th cumulant is given by $\kappa_4 = \mu_4 - 3\mu_2^2$, where μ_4 is the 4th central moment and μ_2 the variance. Assuming promoter at steady state, we solved the equations for 3rd and 4th moments of g and derive the following analytical expressions for 3rd and 4th cumulants, κ_3 and κ_4:

$$\kappa_3 = g_0\langle n\rangle + 3g_0^2\langle n\rangle(1-\langle n\rangle)\Phi_1(\tau_e/\tau_n) + g_0^3\langle n\rangle(1-\langle n\rangle)(1-2\langle n\rangle)\Phi_2(\tau_e/\tau_n) \quad \text{(Equation 9)}$$

$$\kappa_4 = g_0\langle n\rangle + 7g_0^2\langle n\rangle(1-\langle n\rangle)\Phi_1(\tau_e/\tau_n) + 6g_0^3\langle n\rangle(1-\langle n\rangle)(1-2\langle n\rangle)\Phi_2(\tau_e/\tau_n) + g_0^4\langle n\rangle(1-\langle n\rangle)(\Phi_3(\tau_e/\tau_n) - 6\langle n\rangle(1-\langle n\rangle)\Phi_4(\tau_e/\tau_n)) \quad \text{(Equation 10)}$$

where Φ_1, Φ_2, Φ_3 and Φ_4 are noise filtering functions that vanish in the fast switching regime ($\tau_e \gg \tau_n$) and tend to one in the slow switching regime ($\tau_e \ll \tau_n$):

$$\Phi_1(x) = 2\frac{\exp(-x)+x-1}{x^2}$$

$$\Phi_2(x) = 6\frac{x\exp(-x)+2\exp(-x)+x-2}{x^3}$$

$$\Phi_3(x) = 12\frac{x^2\exp(-x)+4x\exp(-x)+6\exp(-x)+2x-6}{x^4}$$

$$\Phi_4(x) = 2\frac{\exp(-x)^2+4x^2\exp(-x)+20x\exp(-x)+28\exp(-x)+10x-29}{x^4}$$

The above expressions for the cumulants are exact and were tested numerically. The cumulants are polynomials of the mean promoter activity $\langle n \rangle$, which follows from the propagation of the binomial cumulants from the switching process. Since the cumulants are extensive, the cumulants for N_g independent gene copies are obtained by multiplying by N_g the expression for a single gene copy (Equations 8, 9, and 10).

Cumulant analysis

Noise-mean relationship and cumulants predicted by the two-state model

Within the context of the two-state model, we tested whether any transcriptional parameter modulations could explain the global trends in the noise and the cumulants (Figures 3A–3D). Since we showed based on the cumulants that the distribution of activity is a single parameter distribution, we restricted the analysis to single parameter modulations of the mean activity (Figures 3F–3I). It is worth mentioning a few important observations that will simplify this task.

First, we see by close inspection of the steady state cumulants (Equations 8, 9, and 10) that τ_e sets the scale, i.e., all parameters are defined with respect to τ_e. In practice, the cumulants only depends on the three following independent parameters $\tilde{k}_{\text{ini}} = k_{\text{ini}}\tau_e$, $\tilde{k}_{\text{on}} = k_{\text{on}}\tau_e$ and $\tilde{k}_{\text{off}} = k_{\text{off}}\tau_e$. Thus, there is some freedom to set the scale of these rates. Here, we used $\tau_e = 2.2$ min that is approximately the Pol II elongation time for the normalized gene length (3.3 kb and $k_{\text{elo}} = 1.5$ kb/min; (Garcia et al., 2013)) and it will be considered fixed. Second, the magnitude of k_{ini} determines whether the Poisson (first term $\propto k_{\text{ini}}$) or the binomial (second term $\propto k_{\text{ini}}^2$) components dominates in the expression of the variance (Equation 6). We immediately see that increasing the mean Pol II number on the gene $\langle g \rangle$ by only modulating k_{ini} cannot explain the data, since it would lead to a monotonic increase of the variance whereas the observed trend is concave with a global maxima at mid-expression levels. The only way of achieving such a trend is by modulating $\langle n \rangle$ provided the binomial term dominates the Poisson one. This condition implies that k_{ini} has to be sufficiently large for intermediate value of $\langle n \rangle$, i.e., $k_{\text{ini}} \gg 1/(\tau_e(1 - \langle n \rangle)\Phi(\tau_e/\tau_n))$. Alternatively, if k_{ini} is known, this inequality sets some constraints on the possible values of τ_n. Third, it is possible to give an estimate of k_{ini} from the polynomial fit of the measured variance (Figure S2A and Figure 3B). The second intercept of the fitted curve (black line) with the Poisson background (dash line), which should occur at $\langle n \rangle = 1$, allows us to estimate g_0. Assuming k_{ini} is maintained constant as $\langle n \rangle$ is modulated, we have $g_0 = k_{\text{ini}}\tau_e = 15.21$, which gives $k_{\text{ini}} = 6.99$ min^{-1} for $\tau_e = 2.2$ min (see above).

We then investigated three different type of single parameter modulation to vary the mean Pol II number $\langle g \rangle$ consistent with the observation above, namely, modulations of the mean occupancy $\langle n \rangle$ from 0 to 1 by either varying k_{on} alone, k_{off} alone or both k_{on} and k_{off} while keeping the switching correlation time τ_n constant. The latter modulation also corresponds to single parameter modulation since $k_{\text{on}} = \langle n \rangle/\tau_n$ and $k_{\text{off}} = (1 - \langle n \rangle)/\tau_n$ are then fully determined by $\langle n \rangle$. For each of these three types of modulation, one parameter is free (either k_{off}, k_{on} or τ_n) and sets the amplitude of the cumulants (Figure S2E). In order to infer these free parameters, we fitted (maximum likelihood) the measured cumulants with the modeled ones (Equations 8, 9, and 10) predicted by each modulation strategy (Figures 3G–3I). We found:

1) k_{on} modulation: $k_{\text{off}} = 0.142$ min^{-1} and $k_{\text{on}} = k_{\text{off}}\langle n \rangle/(1 - \langle n \rangle)$
2) k_{off} modulation: $k_{\text{on}} = 0.075$ min^{-1} and $k_{\text{off}} = k_{\text{on}}(1 - \langle n \rangle)/\langle n \rangle$
3) $\langle n \rangle$ modulation at fixed τ_n: $\tau_n = 2.9993$ min with $k_{\text{on}} = \langle n \rangle/\tau_n$ and $k_{\text{off}} = (1 - \langle n \rangle)/\tau_n$

We then calculated the noise-mean relationship (Equation 2). We also show an example of a k_{ini} modulation alone (Figure 3F, gray line); no matter the value of $\langle n \rangle$ and τ_n this modulation cannot reproduce the trend in the data as explained above. The modulation of k_{off} alone (green line) fails to capture the noise at low expression (Figure 3F). On the other hand both the modulation of k_{on} alone (blue line) and n at constant τ_n (red line) provides good qualitative agreement with the data (Figures 3F–3I). As mentioned above, it is important to keep in mind that the units of k_{ini}, k_{on}, k_{off} and τ_n estimated here depends on the value of the elongation rate. Here, we used a conservative estimate of $k_{\text{elo}} = 1.5$ kb/min (Garcia et al., 2013), which is possibly too small for the gap genes (Fukaya et al., 2017). A different elongation rate would simply imply a rescaling of the rates and the correlation time without affecting the fitting results (STAR methods, *Effect of elongation rate on inference*). Namely, the mean occupancy $\langle n \rangle$ would remain unchanged while the rates would be rescaled by a factor $k^*_{\text{elo}}/k_{\text{elo}}$ and the correlation time by $k_{\text{elo}}/k^*_{\text{elo}}$, where k^*_{elo} corresponds to the new elongation rate.

Time-dependent cumulant analysis

Next, we investigated whether the single parameter modulation fitted above assuming steady state are consistent with the finite duration of the nuclear cycle (approximately 15 min in nc13). Namely, assuming all the data were taken at mid cycle, we asked under each modulation scenario whether steady state could be reached in a timely manner (mid cycle), as supported by our staging analysis (Figures S1A–S1D) and other studies (Garcia et al., 2013). The relaxation time to steady state is determined by the switching correlation time τ_n. By solving the equation for the temporal evolution of the mean Pol II number $\langle g(t) \rangle$ (Equation 5) with initial condition $\langle g(t=0) \rangle = 0$ (no Pol II on the gene) and $\langle n(t=0) \rangle = 0$ (gene initially 'off'), one finds:

$$\langle g(t) \rangle = \begin{cases} g_0\langle n \rangle \left(\frac{t}{\tau_e} + \frac{\tau_n}{\tau_e}(\exp(-t/\tau_n) - 1) \right) t \leq \tau_e \\ g_0\langle n \rangle \left(1 + \frac{\tau_n}{\tau_e}\exp(-t/\tau_n)(1 - \exp(\tau_e/\tau_n)) \right) t > \tau_e \end{cases}$$

As mentioned above, the relaxation of the mean $\langle g(t)\rangle$ to its steady state value $\langle g\rangle = g_0\langle n\rangle$ is determined by the correlation time τ_n through the exponential factor $\exp(-t/\tau_n)$. As τ_n increases, the relaxation gets slower and slower (Figure S3A). It follows that the finite duration of nc13 should set some upper bound on the possible value of τ_n. According to Figure S3A, τ_n should not exceed 3 min for $\langle g(t)\rangle$ to reach approximately 90% of the maximum activity g_0 ($\langle g\rangle = g_0$ for $\langle n\rangle = 1$) at mid cycle as observed in the data (Figure 3B).

Each of the three single parameter modulations fitted above predicts different dependency of τ_n on the mean occupancy $\langle n\rangle$ (Figure S3B). Importantly, these values of τ_n were obtained for $k_{elo} = 1.5$ kb/min (Garcia et al., 2013). A larger elongation rate would lead to smaller correlation times (Fukaya et al., 2017) (STAR methods, *Effect of elongation rate on inference*). The main benefit of using a potentially smaller elongation rate, it provides a stronger guarantee that the time-dependent solution reaches steady state in time (as the relaxation is slower). For each modulation (Figure S3C), we estimated what fraction of the steady state value $\langle g(t)\rangle/\langle g\rangle$ is attained as a function of $\langle n\rangle$ at mid cycle ($t = 7.5$ min). It turns out that the k_{off} modulation clearly fails to reach steady state in time for higher occupancy, whereas both modulation of k_{on} and n at fixed τ_n cover the measured range of activity at mid cycle (0 to 90% of g_0). Each modulation predicts different boundary formation dynamics (Figures S3D–S3F). For k_{on}, the highly expressed regions (large $\langle n\rangle$) relax much faster than the lowly expressed ones (small $\langle n\rangle$), whereas for k_{off} it is the opposite. Interestingly, at fixed τ_n, each position relaxes in synchrony and the activity ratio between them is conserved. The latter modulation appears more consistent with previous experimental observations (Dubuis et al., 2013; Garcia et al., 2013).

Next, we investigated the shape of the higher order time-dependent cumulants. Although the higher order time-dependent cumulants can be calculated from the moment equations, their analytical expressions are cumbersome. Alternatively, one can calculate the time-dependent cumulants directly from the time-dependent distribution of Pol II $P_t(g)$, which is easily computed numerically. With the same initial condition as the mean above, the time-dependent distribution of Pol II $P_t(g)$ is given by:

$$P_t(g) = \begin{cases} \sum_n P_t(g, n \mid g' = 0, n' = 0) & t \le \tau_e \\ \sum_{n,n'} P_{\tau_e}(g, n \mid g' = 0, n') P_{t-\tau_e}(n' \mid n'' = 0) & t > \tau_e \end{cases}$$

where $P_t(g, n \mid g', n')$ is the propagator of the telegraph model (STAR Methods, *Distribution of nascent transcripts*, Equation 12) and $P_t(n \mid n')$ the propagator of the switching process alone:

$$P_t(n, n') = (\delta_{n1}\langle n\rangle + \delta_{n0}(1 - \langle n\rangle))(1 - \exp(-t/\tau_n)) + \delta_{nn'}\exp(-t/\tau_n)$$

We then computed the 2nd, 3rd and 4th time-dependent cumulants from $P_t(g)$ for each fitted modulation (Figure S3G). Provided the elapsed time is sufficiently large compared to the correlation time and the elongation time, the time-dependent cumulants closely follow the steady state solution. Thus, both the modulation of k_{on} alone and n at fixed τ_n fitted assuming steady state predicts time-dependent mean versus cumulant curves at mid cycle ($t = 7.5$ min) that are consistent with the data. In addition, under these conditions, the time-dependent mean activity closely reflect the time-dependent mean occupancy $\langle n(t)\rangle$:

$$\frac{\langle g(t)\rangle}{g_0} = \underbrace{\frac{1 + \frac{\tau_n}{\tau_e}\exp(-t/\tau_n)(1 - \exp(\tau_e/\tau_n))}{1 - \exp(-t/\tau_n)}}_{\approx 1} \langle n(t)\rangle \; t > \tau_e$$

Together it implies that even away from steady state, provided the elapsed time is sufficiently large ($t \gg \tau_e, \tau_n$), the inference based on steady state solutions should yield good estimates of the parameters. Indeed, for fixed τ_e, the relationships between the mean and the cumulants at steady state are uniquely determined by k_{ini}, $\langle n\rangle$ and τ_n. As long as time dependent-cumulants run along the steady state curves (Figure S3G), the estimation of k_{ini} and τ_n will be correct while the estimation of the mean occupancy will in fact correspond to the instantaneous mean occupancy $\langle n(t)\rangle$ as $\langle g(t)\rangle/g_0 \approx \langle n(t)\rangle$.

Inferring transcription kinetics of endogenous genes from dual color smFISH

Dual color smFISH and effective gene length

We performed dual-color smFISH tagging the 5′ and 3′ regions of the transcripts with different probe sets (Figure 4A and Table S1). After normalization in cytoplasmic units, both channels offer a consistent readout of the mean and the variability (Figures S4A and S4B). For each gene, given the 5′ and 3′ FISH probe configurations and assuming constant elongation rate, we calculated the expected ratio of 3′ over 5′ signal $r = C_1^{(3)}/C_1^{(5)}$ according to Equation 3 using the annotated gene length (Figures S4C and S4D and Table S3). The predicted ratios are consistent with the measured ones, albeit with small deviations likely stemming from termination (Figure S4E). This suggests that nascent transcripts might be retained at transcription sites for a short duration. We then calculated for each gene, the effective length that would be consistent with the measured ratio (Figure S4F and Table S3). Assuming an elongation rate $k_{elo} = 1.5$ kb/min (Garcia et al., 2013), we estimated the lag consistent with the length difference between the effective and an-

notated length (Figure S4F inset). Nascent transcripts remain at the loci for at most 35 s, which remains small compared to the typical elongation time for the gap genes $\tau_e \sim 2$ min. In this study, we used the effective elongation time for each gene that includes the short lingering time, which was calculated from the effective gene length.

The two channels enable estimation of the total nascent transcripts (5′ channel) and the fractional occupancy of transcripts along the 5′ and 3′ portions of the gene at each locus (Figures 4B and 4C). Because the 5′ and 3′ activities are temporally correlated through the elongation process additional information about transcription can be extracted that is not available with a single channel/color (Figures 4B and 4D). Combining measurements from multiple embryos (Figures 4C and 4D), we select nuclei at similar positions (bins of 2.5% egg length) to generate the joint distribution of 5′ and 3′ activity across AP position bins (Figure 4D).

Distribution of nascent transcripts

Modeling the joint distribution of 5′ and 3′ activity based on the two-state model requires first to calculate two key distributions, namely the steady-state distribution of nascent transcripts (or Pol II number) on the gene and the propagator that describes the temporal evolution of an arbitrary distribution of nascent transcripts. Both distributions can be derived from the master equation (Equation 4). Although the master equation can be solved using generating functions (Xu et al., 2016), we followed another route that can be easily extended to multi-state system and remains computationally tractable. The master equation can be written in terms of an operator $\widehat{A}$ containing the propensity functions of the different reactions:

$$\frac{d}{dt}P_t(g,n) = \widehat{A}P_t(g,n)$$

After appropriate truncation on the transcript number (setting an upper bound for the maximum number of nascent transcripts) (Munsky and Khammash, 2006), the $\widehat{A}$ operator can be written in terms of a sum of tensor products of different matrices:

$$\widehat{A} = I_G \otimes N_2 + K_G \otimes R_2 \qquad \text{(Equation 11)}$$

with I_G standing for the identity matrix of size $G+1$ where G is the maximum number of transcripts after truncation. The matrix N_2 encodes the rates of the possible transitions for the two-state promoter and R_2 indicates in which promoter state initiation occurs:

$$N_2 = \begin{bmatrix} -k_{\text{on}} & k_{\text{off}} \\ k_{\text{on}} & -k_{\text{off}} \end{bmatrix} R_2 = \begin{bmatrix} 0 & 0 \\ 0 & 1 \end{bmatrix}$$

while K_G describes the initiation of transcripts:

$$K_G = \begin{bmatrix} -k_{\text{ini}} & 0 & 0 & 0 \\ k_{\text{ini}} & \ddots & \ddots & 0 \\ 0 & \ddots & \ddots & 0 \\ 0 & 0 & k_{\text{ini}} & -k_{\text{ini}} \end{bmatrix}$$

The propagator of the resulting finite system can be expressed as a matrix exponential of the $\widehat{A}$ operator:

$$P_t(g,n|g',n',\theta) = \exp\left(\widehat{A}t\right) \qquad \text{(Equation 12)}$$

where θ stands for the set of kinetic parameters $(k_{\text{ini}}, k_{\text{on}}, k_{\text{off}})$. Although the propagator explicitly depends on the kinetic parameters, we chose to omit θ in the following for readability. The propagator dictates how an initial joint distribution of transcript and promoter state $P(g', n')$ evolves after time t in $P(g,n)$:

$$P(g,n) = \sum_{g',n'} P_t(g,n|g',n')P(g',n')$$

The distribution of nascent transcripts $P(g)$ for a gene of length L_g is typically calculated using the propagator above with $t = \tau_e \equiv L_g/k_{\text{elo}}$ the elongation time and the initial conditions. Since τ_e sets the 'memory' of the system, $P(g)$ can be calculated with initially zero nascent transcript on the gene and is then given by:

$$P(g) = \sum_{n,g',n'} P_{\tau_e}(g,n|g',n')\delta_{g'0}P(n') \qquad \text{(Equation 13)}$$

where $P(n)$ specifies the initial distribution of promoter state. The distribution $P(g)$ can be computed efficiently by directly estimating the action of the initial vector on the matrix exponential (Sidje, 1998). Assuming the promoter at steady state, $P(n)$ is then given by:

$$P(n) = \begin{cases} \langle n \rangle \text{ for } n = 1 \\ 1 - \langle n \rangle \text{ for } n = 0 \end{cases}$$

with the mean occupancy $\langle n \rangle = k_{\text{on}}/(k_{\text{on}} + k_{\text{off}})$.

Provided each gene copy is independent and undistinguishable, the combination of two and four gene copies can be represented by a three- and five-state promoter model. The corresponding N and R matrices are given by:

$$N_3 = \begin{bmatrix} -2k_{on} & k_{off} & 0 \\ 2k_{on} & -(k_{off}+k_{on}) & 2k_{off} \\ 0 & k_{on} & -2k_{off} \end{bmatrix} R_3 = \begin{bmatrix} 0 & 0 & 0 \\ 0 & 1 & 0 \\ 0 & 0 & 2 \end{bmatrix}$$

$$N_5 = \begin{bmatrix} -4k_{on} & k_{off} & 0 & 0 & 0 \\ 4k_{on} & -(k_{off}+3k_{on}) & 2k_{off} & 0 & 0 \\ 0 & 3k_{on} & -2(k_{off}+k_{on}) & 3k_{off} & 0 \\ 0 & 0 & 2k_{on} & -(3k_{off}+k_{on}) & 4k_{off} \\ 0 & 0 & 0 & k_{on} & -4k_{off} \end{bmatrix}$$

$$R_5 = \begin{bmatrix} 0 & 0 & 0 & 0 & 0 \\ 0 & 1 & 0 & 0 & 0 \\ 0 & 0 & 2 & 0 & 0 \\ 0 & 0 & 0 & 3 & 0 \\ 0 & 0 & 0 & 0 & 4 \end{bmatrix}$$

The distribution of nascent transcripts is calculated according to Equation 13, with the propagator $P_t(g,n|g',n')$ computed from the updated $\widehat{A}$ operator (Equations 11 and 12). The steady-state distribution of the N_g-gene copy system is given by:

$$P(n) = \binom{N_g}{n} \langle n \rangle^n (1 - \langle n \rangle)^{N_g - n} \text{ with } n \in \{0, 1, 2, \cdots, N_g\} \quad \text{(Equation 14)}$$

where $n = k_{on}/(k_{on}+k_{off})$ is the steady state mean occupancy of a single promoter.

Joint distribution of 5′ and 3′ activity

Here, we lay out the approach used to calculate the joint distribution of 5′ and 3′ activity for an arbitrary configuration of 5′ and 3′ FISH probes. Analytic solutions for steady-state distributions with idealistic single color probe configuration exist (Xu et al., 2016), but solutions for arbitrary probe configurations and multi-color FISH are cumbersome. Here, the computational approach is general enough and can be applied to a large class of transcription model, at or out of steady-state (transient relaxation), provided the elongation process is assumed deterministic.

The measured 5′ and 3′ transcriptional activities result from partially elongated nascent transcripts. Each fluorescent probe is assumed to be instantaneously bound and to contribute equally to the total fluorescence. Thus, the fluorescent signal of each nascent transcript is proportional to the number of probe binding regions that have been transcribed. In order to calculate the joint distribution, one needs to proceed backward in time. Starting from the 3′ end up to the 5′ end of the gene, we accumulate the contribution of nascent transcripts to the signal that could have been initiated in the interval separating two successive probe regions. Since we assumed elongation to occur at constant speed, the distance between two successive probe regions can be converted into a time. Doing so for each interval leads to the following temporal hierarchy (Figure S4G). We used the following naming conventions for the durations $t_i^{(C)}$: the superscript $(C) \in \{(3),(5)\}$ stands for the probe channel, either (3) for the 3′ probes (red channel) or (5) for the 5′ probes (green channel), whereas the subscript i denotes the interval separating probe i from probe $i-1$ where increments are performed along the 3′ end to 5′ end direction.

For instance, if the 5′ and 3′ signal is measured at time $t = \tau_e$, only transcripts initiated during the time interval $[0, t_1^{(3)}]$ fully contribute (1 C.U.) to the 3′ (red) signal, since only those get fully bound by 3′ FISH probes. On the other hand, transcripts initiated during $[t_1^{(3)}, t_1^{(3)} + t_2^{(3)}]$ will contribute less to the signal since the last probe region has not yet been transcribed at the time of the measurement $t = \tau_e$. Thus, the individual contribution of these transcripts to the total 3′ signal is $(k-1)/k$ C.U., where k is the total number of probes for the 3′ channel. As we will see below, the probability to initiate g nascent transcripts during any duration $t_i^{(C)}$ is given by the propagator $P_{t_i^{(C)}}(g,n|0,n')$ (Equation 12), where n and n' are the promoter states before and after $t_i^{(C)}$.

For any model of promoter activity that only consider the stochastic initiation of transcripts (as a Poisson process) and deterministic elongation with instantaneous release, the propagator will satisfy the following equality:

$$P_t(g,n|g',n') = P_t(g-g',n|0,n')$$

Thus, one only needs to calculate $P_t(g,n|0,n') \equiv P_t(g,n|n')$, which can be computed much faster than the matrix exponential (Equation 12) (Sidje, 1998). It then follows that the Chapman-Kolmogorov equation for the time propagation reduces to a discrete convolution:

$$P_{t_2+t_1}(g_2,n_2|n_0) = \sum_{n_1} \sum_{g_1=0}^{g_2} P_{t_2}(g_2-g_1,n_2|n_1) P_{t_1}(g_1,n_1|n_0)$$

This property is used extensively in the following calculation of the joint distribution.

The computation of the joint distribution is performed according to a dynamic programming approach that can in principle be applied to an arbitrary number of color probes. We first calculate recursively the 3′ contribution (red probes) to the signal $P^{(3)}(\tilde{G}_k, G_k, n_k)$, where $\tilde{G}_k$ stands for the total signal in probe space, G_k the total number of nascent transcripts, n_k the promoter state and k the total number of probes covering the 3′ region. We then calculate the 5′ contribution in a similar fashion, $P^{(5)}(\tilde{G}_k, n_0)$. Lastly, we combine both components to generate the final joint distribution $P(\tilde{G}^{(5)}, \tilde{G}^{(3)})$ in probe space.

Step 1: calculate the 3′ contribution. The initial distribution is given by:

$$P^{(3)}\left(\tilde{G}_2, G_2, n_2\right) = P^{(3)}\left(\overbrace{(k-1)g_2 + kg_1}^{\&doublehyphen;38pt\tilde{G}_2}, \overbrace{g_2+g_1}^{G_2}, n_2\right) = \sum_{n_0,n_1} P_{t_2^{(3)}}(g_2, n_2|n_1) P_{t_1^{(3)}}(g_1, n_1|n_0) P(n_1) P(n_0)$$

where $P(n_0)$ and $P(n_1)$ are the initial distributions of promoter state at time $t_0 = 0$ and $t_1^{(3)}$ respectively. Assuming promoters at steady state, both distributions are then given by Equation 14 for a multi-gene system. We then perform the following recursion scheme for $i = \{3, \cdots, k\}$:

$$P^{(3)}\left(\tilde{G}_i, G_i, n_i\right) = \sum_{n_{i-1}} \sum_{g_i=0}^{g_{\max}} P_{t_i^{(3)}}(g_i, n_i|n_{i-1}) P^{(3)}\left(\underbrace{\tilde{G}_i - (k-i+1)g_i}_{\tilde{G}_{i-1}}, \underbrace{G_i - g_i}_{G_i}, n_{i-1}\right)$$

where $g_{\max} = \min\left(\lfloor \tilde{G}_i/(k-i+1) \rfloor, G_i\right)$.

Step 2: calculate the 5′ contribution. The initial distribution is given by:

$$P^{(5)}\left(\tilde{G}_1, n_1|n_0\right) \equiv P^{(5)}(kg_1, n_1|n_0) = P_{t_1^{(5)}}(g_1, n_1 \mid n_0)$$

We then perform the following recursion scheme for $i = \{2, \cdots, k\}$:

$$P^{(5)}\left(\tilde{G}_i, n_i|n_0\right) = \sum_{n_{i-1}} \sum_{g_i=0}^{g_{\max}} P_{t_i^{(5)}}(g_i, n_i \mid n_{i-1}) P^{(5)}\left(\underbrace{\tilde{G}_i - (k-i+1)g_i}_{\tilde{G}_{i-1}}, n_{i-1}|n_0\right)$$

where $g_{\max} = \lfloor \tilde{G}_i/(k-i+1) \rfloor$. Lastly, we sum out n_k:

$$P^{(5)}\left(\tilde{G}_k|n_0\right) = \sum_{n_k} P^{(5)}\left(\tilde{G}_k, n_k|n_0\right)$$

Step 3: combine 3′ and 5′ contributions. The final joint distribution of 5′ and 3′ activity in probe space is then given by:

$$P\left(\tilde{G}^{(5)}, \tilde{G}^{(3)}\right) = \sum_{n} \sum_{G=0}^{G_{\max}} P^{(5)}\left(\tilde{G}^{(5)} - kG|n\right) P^{(3)}\left(\tilde{G}^{(3)}, G, n\right)$$

where $G_{\max} = \left\lfloor \tilde{G}^{(5)}/k \right\rfloor$. $P^{(3)}$ and $P^{(5)}$ are the joint distributions computed at step 1 and 2. Since the actual signal resolution is of the order of 1 cytoplasmic unit (a fully tagged transcript with k fluorescent probes), the joint distribution can be coarse-grained by aggregating the states $\tilde{G}$ by a block of size k corresponding to a single cytoplasmic unit. The coarse-grained distribution will be denoted $P(G^{(5)}, G^{(3)})$ in the following. In addition, it is possible to compute $P(G^{(5)}, G^{(3)})$ faster and with good accuracy using a reduced effective number of probes k, provided the original probe configuration is well approximated. Lastly, we remind the readers that $P(G^{(5)}, G^{(3)})$implicitly depends on the kinetic parameters $(k_{\text{ini}}, k_{\text{on}}, k_{\text{off}})$ through the two-state model propagator, the elongation rate and the position of the probes through the temporal hierarchy (Figure S4G).

Likelihood and inference

We modeled the joint distribution of 5′ and 3′ activity based on the two-state model and the exact probe location assuming steady state and constant Pol II elongation rate (Figure 4E; STAR Methods, *Joint distribution of 5′ and 3′ activity*). The resulting modeled activity distribution, together with the measurement noise model (Figure 2A; STAR Methods, *Imaging noise model*), enable calculating the likelihood of the 5′ and 3′ activities in C.U. (i.e., Data) given a set of kinetic parameters $(k_{\text{ini}}, k_{\text{on}}, k_{\text{off}})$. Specifically, the likelihood of the data $\text{Data} = \{S^{(5)}, S^{(3)}\}$ given the parameters $\theta = (k_{\text{ini}}, k_{\text{on}}, k_{\text{off}})$ is expressed in terms of the measurement noise model $P(S^{(5)}, S^{(3)}|G^{(5)}, G^{(3)})$ (Equation 1) and the joint distribution $P(G^{(5)}, G^{(3)} \mid \theta)$:

$$P(\text{Data}|\theta) = \prod_{i=1}^{N_D} \sum_{G^{(5)}, G^{(3)}} P\left(S_i^{(5)}, S_i^{(3)}|G^{(5)}, G^{(3)}\right) P\left(G^{(5)}, G^{(3)} \mid \theta\right)$$

where N_D is the total amount of data, i.e., the total number of measured nuclei per AP-bin for a given gene.

The general idea underlying "classical" inference is to maximize the probability of the data under some model, namely to find the parameters $(k_{ini}, k_{on}, k_{off})$ that maximize the likelihood of the data $P(\text{Data}|k_{ini}, k_{on}, k_{off})$. In this manuscript we adopted a Bayesian approach, estimating the probability of the kinetic rate parameters of the two-state model given the observed data (i.e., the joint posterior distribution) $P(k_{ini}, k_{on}, k_{off}|\text{Data})$ using Bayes' rule:

$$P(k_{ini}, k_{on}, k_{off}|\text{Data}) = \frac{P(\text{Data}|k_{ini}, k_{on}, k_{off})P(k_{ini}, k_{on}, k_{off})}{P(\text{Data}) \equiv \int P(\text{Data}|k_{ini}, k_{on}, k_{off})P(k_{ini}, k_{on}, k_{off})dk_{ini}dk_{on}dk_{off}}$$

where $P(k_{ini}, k_{on}, k_{off})$ is the prior that encodes for prior knowledge about the parameter values. We used a non-informative and independent prior for each kinetic parameter, which was chosen as log-uniform $P(k_{ini}, k_{on}, k_{off}) = 1/(k_{ini} \cdot k_{on} \cdot k_{off})$. Note that in absence of a prior $P(k_{ini}, k_{on}, k_{off})$, the most likely parameters are the ones that maximize $P(\text{Data}|k_{ini}, k_{on}, k_{off})$. In that case, the Bayesian approach is essentially equivalent to "classical" maximum likelihood. The main advantage of the Bayesian approach over maximum likelihood is that it provides a natural way to estimate the uncertainty on the parameters through the joint posterior and allows us to determine whether the parameters are identifiable. Indeed, as the uncertainty grows, the posterior distribution becomes wider/flatter, which directly reflects on the range of the parameter confidence intervals.

Importantly, we set the elongation rate k_{elo} to the experimentally measured value of 1.5 kb/min (Garcia et al., 2013). At steady state, a known value of k_{elo} is required to set the temporal scale of the other transcriptional parameters, which can be seen by inspecting the expressions of the various cumulants of the nascent transcript distribution (Equations 8, 9, and 10). Since all cumulants can be parameterized by the three independent parameters $g_0 = k_{ini}/k_{elo}$, $n = k_{on}/(k_{on} + k_{off})$ and the ratio $\tau_e/\tau_n = (k_{on} + k_{off})/k_{elo}$, it follows that the model is not identifiable when the temporal scale is not set.

We then sampled the joint posterior distribution $P(k_{ini}, k_{on}, k_{off}|\text{Data})$ using a Markov chain Monte Carlo (MCMC) algorithm (Hastings, 1970), for each gene and at each AP position individually. The sampled joint posterior distribution enables estimation of the marginal posterior distribution for each kinetic rate and any combination of these rates, such as $\langle n \rangle$ and τ_n. All the parameters of the model and the error bars were estimated from the marginal posterior distribution, as the median and the percentiles respectively (Figure 4E). The best-fitting distributions predicted by the model match the data closely (Figure S5B), and outliers are mainly explained by measurement and binning noise. Importantly, our inference approach does not require any *a priori* assumptions about the underlying parameter modulation, nor does it assume any continuity between datasets. In principle, the inferred parameters could be different for each gene and be modulated in any arbitrary way.

Parameter identifiability and performance

As mentioned above, the two-state model is fully identifiable (structural identifiability) as long as k_{elo} is fixed. Indeed, in that case the steady state and time-dependent solution depend on three independent parameters, such as $(k_{ini}, k_{on}, k_{off})$ or $(k_{ini}, \langle n \rangle, \tau_n)$. In principle, provided one has enough data and measurement noise is small, each parameter can be resolved individually. On the other hand, it is true that some regimes might require a very large/infinite amount of data to infer the different parameters without ambiguity (practical identifiability). For instance, in the case of instantaneous bursts, namely when k_{off} and k_{ini} become large (i.e., approach infinity, but with finite ratio), only the burst size $b = k_{ini}/k_{off}$ and the burst frequency $f = k_{on}$ are well defined. Thus it is not possible to infer the exact values of k_{ini} and k_{off} individually. Such a scenario can be clearly diagnosed based on the marginal posterior distributions $P(k_{ini}|\text{Data})$ and $P(k_{off}|\text{Data})$ (from which the median and the error bars of the parameters are estimated). Indeed, since we used non-informative priors, the variance of these marginal posterior distributions would become extremely large and thus less informative. More intuitively, k_{ini} and k_{off} would no longer be sharply peaked around a mean value, but would take all possible values (consistent with the prior) that satisfy $b = k_{ini}/k_{off} \pm$ some error on b. This would consequently lead to to very large error bars on k_{ini} and k_{off}. Thus, the error bars extracted from the marginal posterior distribution are indicative for whether or not we can estimate these parameters.

To validate our inference framework, we tested the inference on simulated data using a broad range of parameter values and in presence of measurement noise. Using the Gillespie algorithm (Gillespie, 1977), we generated simulated nuclei activity data based on 4 independent gene copies modeled by the telegraph model. We used the probe configuration and gene length of *hb* and assumed a typical elongation rate of 1.5 kb/min (Garcia et al., 2013). Measurement noise was included in the simulated data according to the characterization performed previously on real data (*Imaging noise model*). We investigated different parameter regimes and modulation schemes of the mean activity $\langle g \rangle$, to test whether the input parameters used to generate the data could be inferred properly (Figures S6A–S6E). Namely, we tested:

1) Modulation of the initiation rate k_{ini} alone with $\tau_n = 2$ min and $\langle n \rangle = 0.35$ (cyan dash line).
2) Modulation of the on-rate k_{on} alone with $k_{ini} = 7$ min^{-1} and $k_{off} = 0.25$ min^{-1} (green dash line).
3) Modulation of the off-rate k_{off} alone with $k_{ini} = 7$ min^{-1} and $k_{on} = 0.25$ min^{-1} (blue dash line).
4) Modulation of the mean occupancy $\langle n \rangle$ alone with $k_{ini} = 7$ min^{-1} and $\tau_n = 2$ min (red dash line).

For each scenario, we generated 8 batches of data covering the range of normalized activity $\langle g \rangle / g_0$. Each batch was made of 10 independently sampled datasets of 500 nuclei activity measurements. We performed the inference on each dataset individually and reported the mixture of posterior distribution over the 10 datasets to take into account the finite size variability in the generated data. We conclude that the inference framework performs well, since all the inferred quantities cover the true values within error bars.

In addition, we estimated globally for all synthetic data the fractional inference error $|\theta_{inf} - \theta_{true}|/\theta_{true}$ from the MCMC sampled parameters θ_{inf}. For all inferred parameters, the median of the error never exceeds 20% (S6F). Overall, the inference allows us to distinguish the different tested modulation strategies without ambiguities. In addition, the sampled joint posterior distributions $P(k_{ini}, k_{on}, k_{off}|\text{Data})$ are clearly peaked in the parameter space (Figure S5C), indicating that practical identifiability is not an issue with real data.

Effect of elongation rate on inference

As discussed above, the elongation rate k_{elo} sets the temporal scale of the transcriptional parameters, thus a different elongation rate would lead to different values of the parameters. In the manuscript, we used a value of $k_{elo} = 1.5$ kb/min which we previously measured (Garcia et al., 2013). A recent study suggests that this value might be overall larger in the blastoderm embryo, of the order of 2.5 kb/min (Fukaya et al., 2017). We thus sought to determine to which extent this new value would affect our results.

In principle, a different value of k_{elo} rescales the transcriptional parameters in a very predictable way. No matter the elongation rate, the three quantities k_{ini}, $\langle n \rangle$ and τ_n should be perfectly identifiable. It follows that the new parameters (denoted by the * superscript) have to satisfy the following equations:

$$k_{ini}\frac{k^*_{elo}}{k_{elo}} = k^*_{ini}$$

$$\langle n \rangle = \langle n \rangle *$$

$$\tau_n \frac{k_{elo}}{k^*_{elo}} = \tau^*_n$$

Inferring the transcriptional parameters from the data with $k_{elo} = 2.5$ kb/min instead of $k_{elo} = 1.5$ kb/min (as in the main text) confirms the rescaling above (Figures S6L–S6N). As predicted, k_{ini} and k_{ini} are rescaled by a factor $2.5/1.5 = 1.67$ and $1.5/2.5 = 0.6$ respectively, whereas $\langle n \rangle$ is conserved.

QUANTIFICATION AND STATISTICAL ANALYSIS

We imaged *hunchback* wild-type (labeled *hb* wt) in N = 18 embryos; a *hunchback* deficiency fly line with half the *hb* dosage (*hb* def) N = 7; *Krüppel* (*Kr*) N = 11; *knirps* during early (*kni* early) N = 14 and late nc13 (*kni* late) N = 16; *giant* females with two alleles (*gt* female) N = 20 and *giant* males with one allele (*gt* male) N = 16. On average the number of quantified nuclei per AP bin (2.5% egg length) is n = 499 (*hb* wt), n = 157 (*hb* def), n = 270 (*Kr*), n = 354 (*kni* early), n = 302 (*kni* late), n = 397 (*gt* female anterior region), n = 387 (*gt* female posterior region), n = 310 (*gt* male anterior region) and n = 277 (*gt* male posterior region). The confidence intervals for all point estimators of the data (mean, variance, noise, third cumulant and fourth cumulant; Figures 1, 2, and 3) were built by bootstrapping the empirical distribution of activity in each individual embryo. We used the 68% confidence intervals for the point estimators. All the error bars for the inferred parameters (Figure 5) correspond to the 10^{th} to 90^{th} percentiles of the marginal posterior distributions.

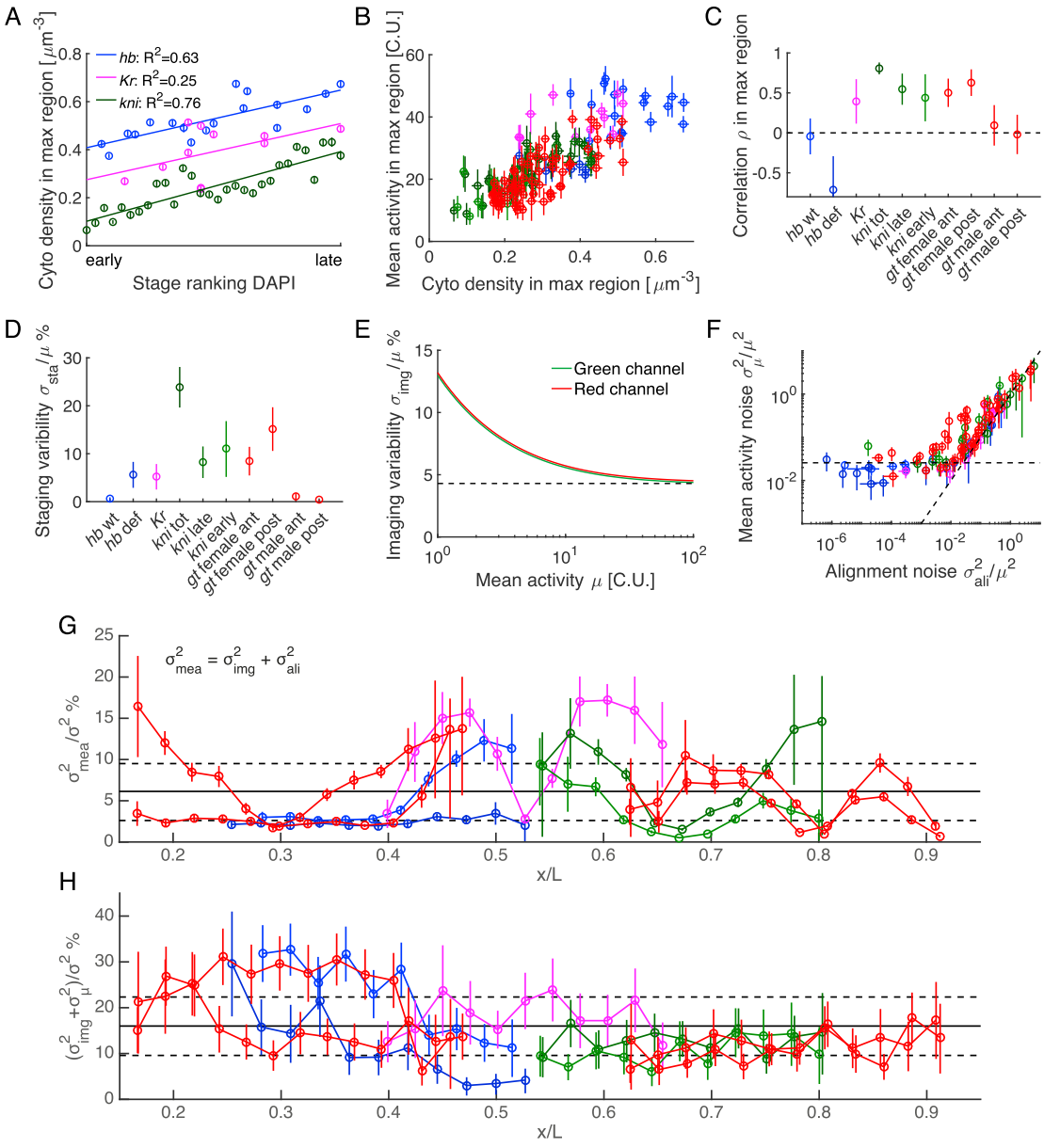

Figure S1. Temporal Staging, Measurement Error, and Embryo-to-Embryo Variability, Related to Figures 1 and 2

(A) Cytoplasmic mRNA density as a function of developmental stage during the 13th interphase as estimated from DAPI staining by eye-inspection. Each data point corresponds to a single embryo; cytoplasmic density was measured for each gene in the maximally expressed spatial region along the AP axis. Good correlation between manual ranking and the cytoplasmic mRNA accumulation correlation justifies the latter as a convenient proxy for time, and thus the developmental age of the embryos within nuclear cycle 13.

(B) Mean activity in the maximally expressed regions as a function of the cytoplasmic mRNA density. Each data point corresponds to a single embryo. Color code as in Figure 1C.

(C) Pearson correlation coefficient ρ between the mean activity and the cytoplasmic mRNA density calculated over the population of embryos in (B). Values indicate that up to 44% (ρ^2) of the variance in mean activity across embryos can be explained by staging uncertainty. The large correlation for *kni* (dark green) led to splitting the population of *kni* stained embryos into early and late stages to minimize the staging uncertainty in each subpopulation. We performed the splitting by finding the cytoplasmic density threshold that minimizes the sum of within-population variance in mean activity.

(D) Staging variability σ_{sta} in percent of the total mean activity μ for each gene in the respective maximally expressed regions. The staging variability corresponds to the variability in mean activity among embryos, which is explained by staging uncertainty between early and late embryo as estimated from cytoplasmic mRNA density. The staging variability σ_{sta} is defined as $\sigma_{sta} = \rho\sigma_\mu$, where σ_μ is the standard deviation of the mean activity across embryos. Note that the splitting of *kni* stained embryos into early and late stages was justified as the staging variability is significantly reduced. The overall small staging variability, which never exceeds 14%, indicates that the mean activity is sufficiently stable in time to warrant a steady state assumption.

(legend continued on next page)

(E) Modeled imaging noise (CV) as a function of the mean activity for both channels. The imaging noise model was built from dual-color smFISH data using an alternating probe configuration (see Figure 2A). Imaging error σ_{img} was determined from the spread along the regression line between both channels (STAR Methods). Errors were assumed normally distributed, independent, and of equal magnitude in both channels. Thus, the modeled imaging error σ_{img} is characterized as the orthogonal spread along the fitted regression line, which was parameterized as $\sigma_{img}(v) = \sqrt{\sigma_b^2 + b_1 v + b_2 v^2}$, where (σ_b^2, b_1, b_2) are fit parameters, and v is the scalar projection of each data point onto the regression line. After fitting, the modeled imaging noise (CV) is given by $\sigma_{img}(v)/\mu$ with $v = \sqrt{\mu^2 + (a\mu)^2}$ for the green channel (green line) and $v = \sqrt{\mu^2 + (\mu/a)^2}$ for the red channel (red line), where a is the slope of the fitted line and μ is the mean activity.

(F) Variability of the mean across embryos (CV^2) as a function of alignment noise. Each data point corresponds to a single AP bin (2.5% egg length). The diagonal dashed line (slope = 1) highlights the correlation between the two quantities at the boundaries while the horizontal dash line corresponds to the embryo variability in the maximally expressed regions for each gene (Figure 2E). The correlation indicates that most variability across embryos in the transition regions can be explained by alignment noise, whereas the remaining variability in the maximally expressed regions reflects staging variability (C and D) and other extrinsic noise sources.

(G) Fraction of the total variance σ^2 corresponding to the measurement variance as a function of the AP position. Measurement variability σ^2_{mea} is defined as the combination of imaging σ^2_{img} and alignment variability σ^2_{ali} . The solid and dashed vertical lines are the overall mean fraction across genes and the 68% confidence interval, respectively.

(H) Fraction of the total variance σ^2 corresponding to the non-nuclear variance as a function of the AP position. The non-nuclear variance is the sum of the imaging σ^2_{img}, the alignment σ^2_{ali} and embryo variability σ^2_{emb}. The remaining variance $\sigma^2_{nuc} = \sigma^2 - \sigma^2_{img} - \sigma^2_{ali} - \sigma^2_{emb}$ is defined as the *nuclear variance* and is deemed intrinsic to transcription. Overall, the nuclear variance largely predominates as it represents 84% of the total variance, on average. The solid and dashed vertical lines are the overall mean fraction across genes and the 68% confidence interval. Color code as in Figure 1C.

All error bars are the 68% confidence intervals.

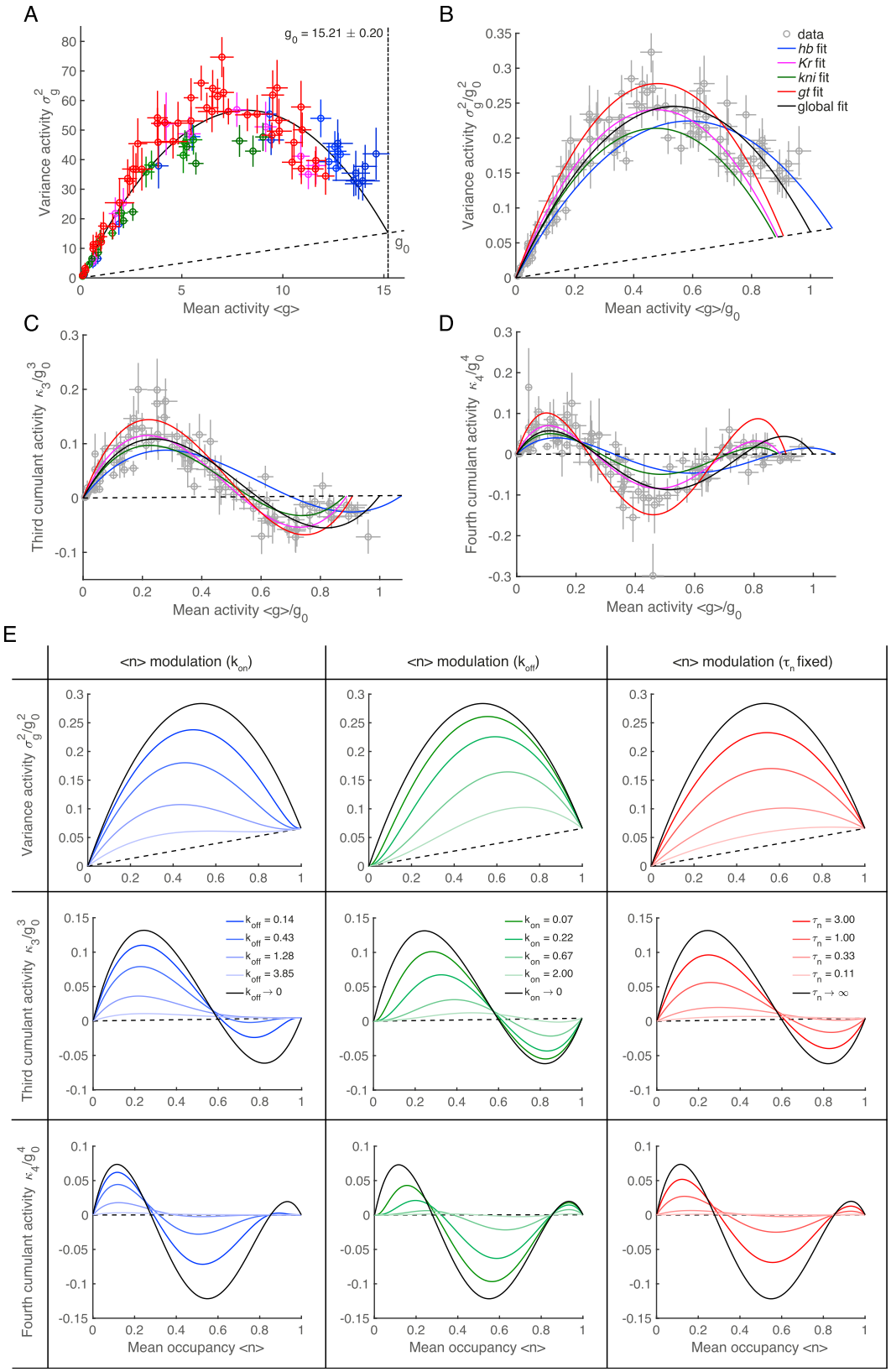

(legend on next page)

Figure S2. Mean-Cumulant Activity Relationships for a Single Gene Copy, Related to Figure 3

(A–D) The mean and the cumulants were corrected for different gene length, probe configuration and copy number. Each data point corresponds to a single AP bin and the error bars are the 68% confidence intervals. The dashed line stands for the Poisson background. Color code as in Figure 1C.

(A) Estimation of the maximal activity g_0 by fitting a 2nd order polynomial of the mean activity to the variance. The maximal activity g_0 is determined as the second intercept of the fit with the Poisson background (vertical dashed line). In Figures 3B–3D and S2B-D the mean and the cumulants are normalized by the respective powers of g_0. Notably, $\langle g \rangle / g_0 = \langle n \rangle$ for constant k_{ini}.

(B–D) Normalized cumulants as a function of normalized mean activity. The solid lines are 2nd (B), 3rd(C) and 4th (D) order polynomial fits, respectively. Fits were performed for each gene independently (colored lines); black line corresponds to the global fit of all genes (Figures 3B–3D). Individual fits are qualitatively similar, suggesting global trends in the data.

(E) Steady state two-state model cumulants as a function of the mean occupancy $\langle g \rangle / g_0 = \langle n \rangle$ for different scenarios of single parameter modulation (modulation of $\langle n \rangle$ through either k_{on} or k_{off} alone, or modulation of $\langle n \rangle$ at fixed correlation time τ_n by changing both k_{on} and k_{off}; Figures 3G–3I). For each considered modulation, only a single parameter is free since the value of g_0 (determined from A) has been fixed and the initiation rate k_{ini} is assumed constant. Varying the free parameters (graded colored lines) mainly affects the amplitude of the cumulants. The solid black lines stand for the common maximal amplitude limit attained when the correlation time goes to infinity.

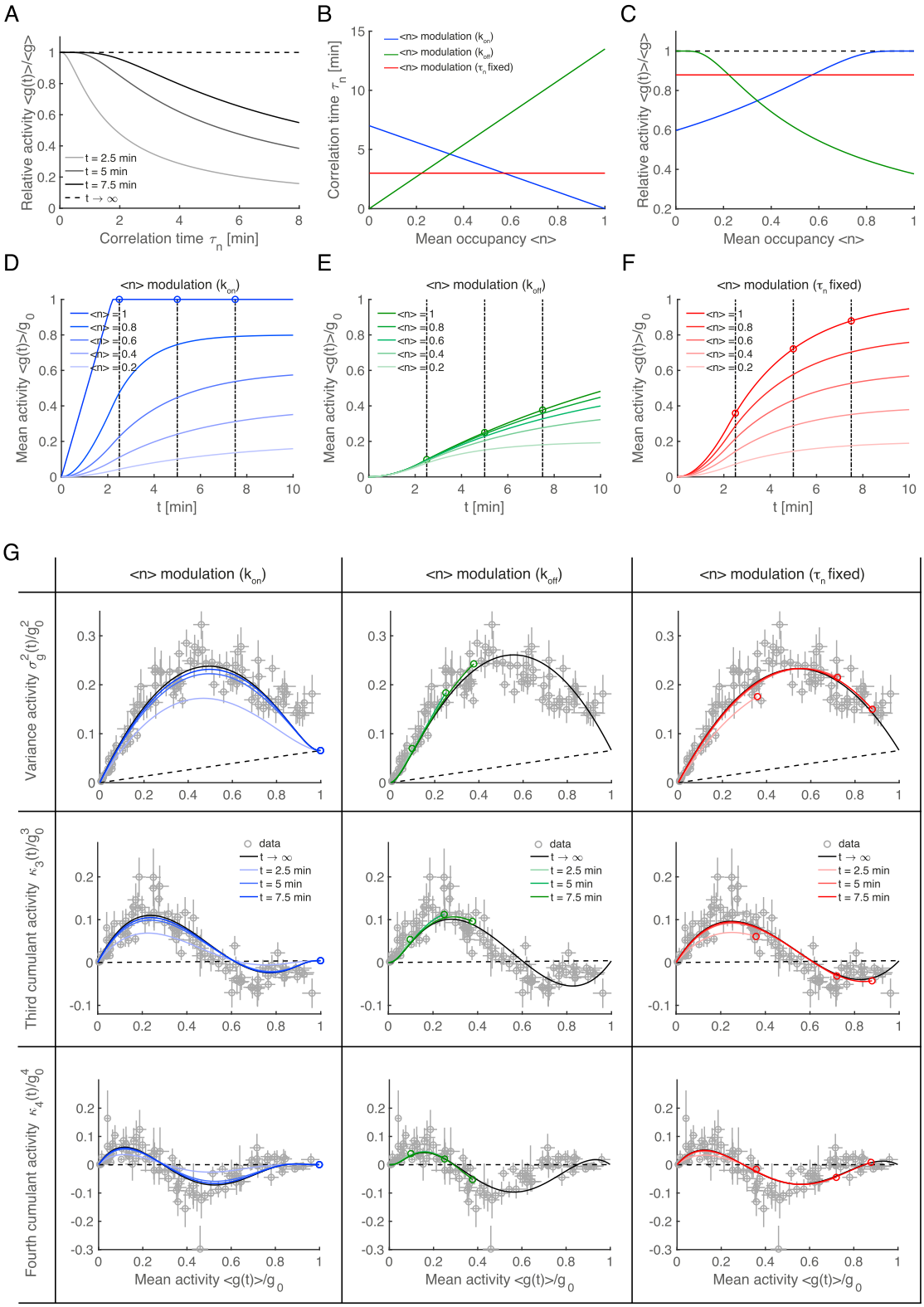

Figure S3. Time-Dependent Cumulant Analysis, Related to Figure 3

All time dependent-solutions of the two-state model were calculated with initial conditions $g(t=0)=0$ (no Pol II on the gene) and $n(t=0)=0$ (gene initially in the 'off' state).

(legend continued on next page)

(A) Time-dependent mean activity $\langle g(t)\rangle$ normalized by its steady state value $g(t\rightarrow\infty)\equiv g$ at three different times ($t = 2.5$ min, $t = 5$ min and $t = 7.5$ min) as a function of the switching correlation time τ_n. At steady state, the ratio is thus equal to one (horizontal dashed line). The correlation time is the only parameter that affects the relaxation to steady state. As τ_n increases, the relaxation becomes slower. For $t = 7.5$ min, a correlation time no larger than 3 min is required to reach approximately 90% of the maximal activity as observed in the data (Figure 3B).

(B) Correlation time τ_n as a function of the mean occupancy $\langle n\rangle$ for each best-fit single parameter modulation (from Figures 3G–3I). Modulation of k_{off} alone predicts a correlation time that is too large ($\tau_n \gg 3$ min) at high $\langle n\rangle$ to reach the maximal activity of the data at mid cycle (7.5 min).

(C) Time-dependent relative activity as a function of the mean occupancy $\langle n\rangle$ for each best-fit single parameter modulation (as in Figures 3G–3I). Same color code as in (B). The relative activity was calculated as the mean activity $\langle g(t)\rangle$ at $t = 7.5$ min normalized by its steady state value $\langle g\rangle$. Modulation of k_{off} alone clearly fails to reach steady state in time at high $\langle n\rangle$, as it only reaches 40% of the maximal activity. On the other hand, both modulation of k_{on} alone and of $\langle n\rangle$ at fixed τ_n reach a sufficiently large maximal activity to explain the data (100% and 88%, respectively).

(D–F) Normalized time-dependent mean activity $\langle g(t)\rangle/g_0$ as a function of time for each best-fit single parameter modulation (as in Figures 3G–3I). The circles correspond to the maximal attainable activity ($\langle n\rangle = 1$) after $t = 2.5, 5$ and 7.5 min (vertical dashed lines). Each modulation predicts different dynamics for boundary formation; for k_{on} modulation high $\langle n\rangle$ regions relax faster than low $\langle n\rangle$ regions (D), while it is the opposite for k_{off} (E). For fixed τ_n, all regions relax in synchrony independently of $\langle n\rangle$ (F). In the latter case, during interphase 13 the ratio of any two curves is constant in time, and thus these ratios are conserved across the patterning boundaries, which are uniquely determined by $\langle n\rangle$.

(G) Normalized time-dependent cumulants as a function of the normalized time-dependent mean activity for each best-fit single parameter modulation. The solid black lines correspond to the steady state best fits in Figures 3G–3I. The data in gray are identical to Figures 3B–3D and the error bars are given by the 68% confidence intervals. For sufficiently large t (i.e., $t > \{\tau_n, \tau_e\}$), the time-dependent mean and cumulant relationships closely follow the steady state ones. In addition, at fixed elongation time τ_e, the set of steady state cumulants are uniquely determined by k_{ini}, $\langle n\rangle$ and τ_n. Together, these two observations imply that even when far from steady state, fitting the steady state cumulants would still provide good estimates of the parameters, except that the estimated $\langle n\rangle$ would instead corresponds to the instantaneous mean occupancy $\langle n(t)\rangle \approx \langle g(t)\rangle/g_0$ (STAR Methods).

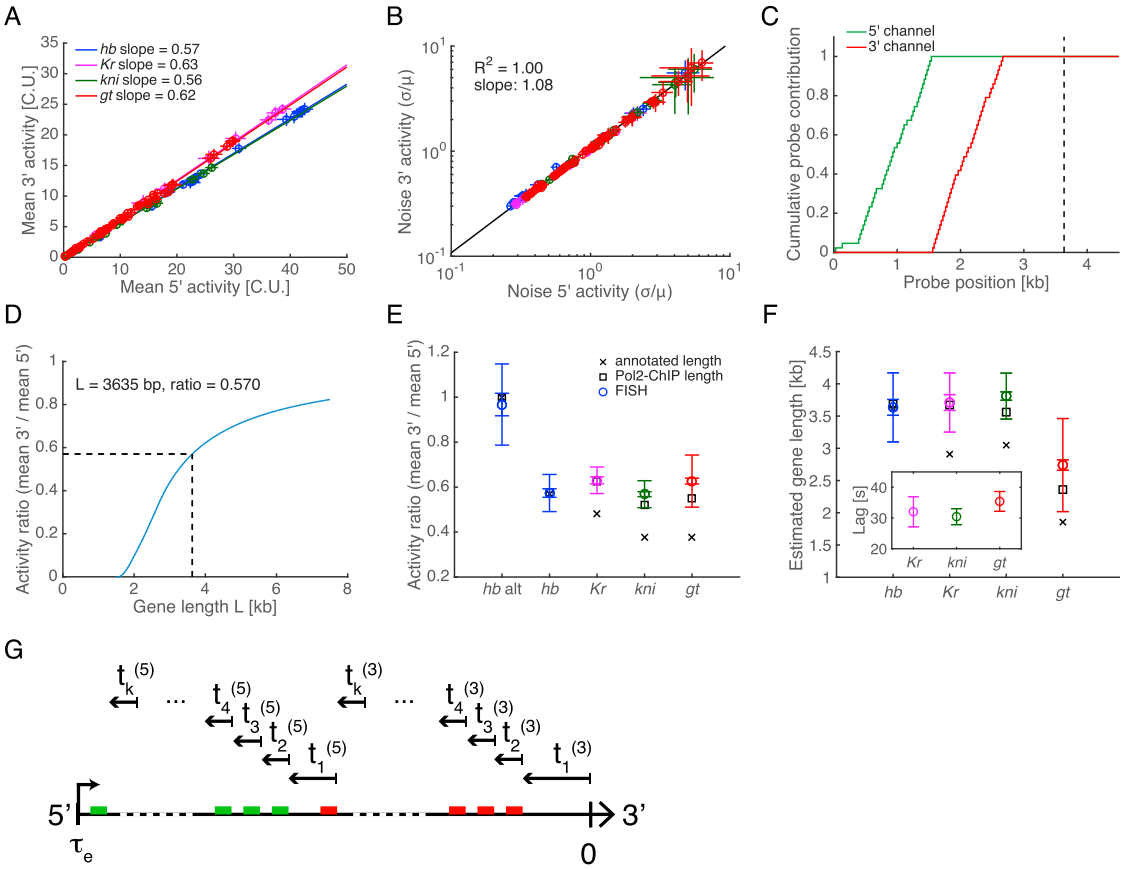

Figure S4. Link between Signal Properties from Dual-Color smFISH and Probe Configuration for Each Gene, Related to Figure 4

(A) Mean 3′ versus 5′ activity for all gap genes. Each data point corresponds to the mean activity over all embryos in a single AP bin. The slopes for the different genes depend on the exact probe configuration. Error bars are the 68% confidence intervals.

(B) 3′ versus 5′ noise (CV). The excellent correlation and the slope close to one suggest that the switching correlation time τ_n is on the order of the elongation time τ_e. Indeed, if $\tau_n < \tau_e$, one would have expected more buffering of the switching noise on the 5′ end compared to the 3′ end, whereas if $\tau_n \gtrsim \tau_e$ the magnitude of the noise should be similar on both ends. Error bars as in (A).

(C) Cumulative *hb* probe contribution to the fluorescence signal as a function of transcript length. The vertical dashed line corresponds to the length of a cytoplasmic mRNA for *hb* (3635 bp). Transcripts whose length is larger than 2667 bp would contribute as 1 cytoplasmic unit in both channels.

(D) Activity ratio (mean 3′ signal over mean 5′ signal) as a function of gene length for *hb* (blue line). Assuming elongation to occur at constant speed and instantaneous release of transcripts, the ratio is fully determined by the probes' location and the gene length (transcribed region). The activity ratio results from the ratio of the integrals of the cumulative probe contribution in (C).

(E) Activity ratio for each gene. The circles stand for the measured ratio with error bars (both standard errors and standard deviations are shown) obtained from the propagation of the normalization errors in both channels for all embryos. The crosses correspond to the predicted ratio based on the annotated gene length. The squares are derived from Pol2 occupancy data (Pol2-ChIP; Blythe and Wieschaus, 2015). For *Kr*, *kni* and *gt*, Pol2 signal is found a few hundreds bp away from the annotated length suggesting extra processing related to termination. Similarly, the larger measured ratios (compared to the predicted ones based on annotated gene length (crosses)) likely reflect retention of nascent transcripts at the loci due to termination.

(F) Effective gene length for each gene as determined from the activity ratio. Symbols and error bars as in (E). Assuming an elongation speed of 1.5 kb/min, the difference between the effective and annotated gene length can be translated in time (inset). The lag or extra residence time of transcripts at the loci is at most 35 seconds.

(G) Temporal hierarchy used to calculate the 5′ and 3′ joint distribution of transcriptional activities. The measured signal result from partially tagged nascent transcripts and is proportional to the number of probe binding regions that have been transcribed. In order to calculate the joint distribution, we accumulate the distinct contribution of nascent transcripts, between each probe region, from the 3′ end up to the 5′ end of the gene. At constant elongation rate, the distance separating each successive probe region is converted into a time $t_i^{(C)}$, where the superscript $(C) \in \{(3),(5)\}$ stands for the probe channel and the subscript i denotes the interval separating probe i from probe $i-1$ (from the 3′ end to 5′ end direction). The joint distribution of activity is obtained by subsequent convolution of the distribution of Pol II initiated during each time $t_i^{(C)}$. Each of these convolutions are properly weighted to take into account the proper contribution of each probe region to the activity.

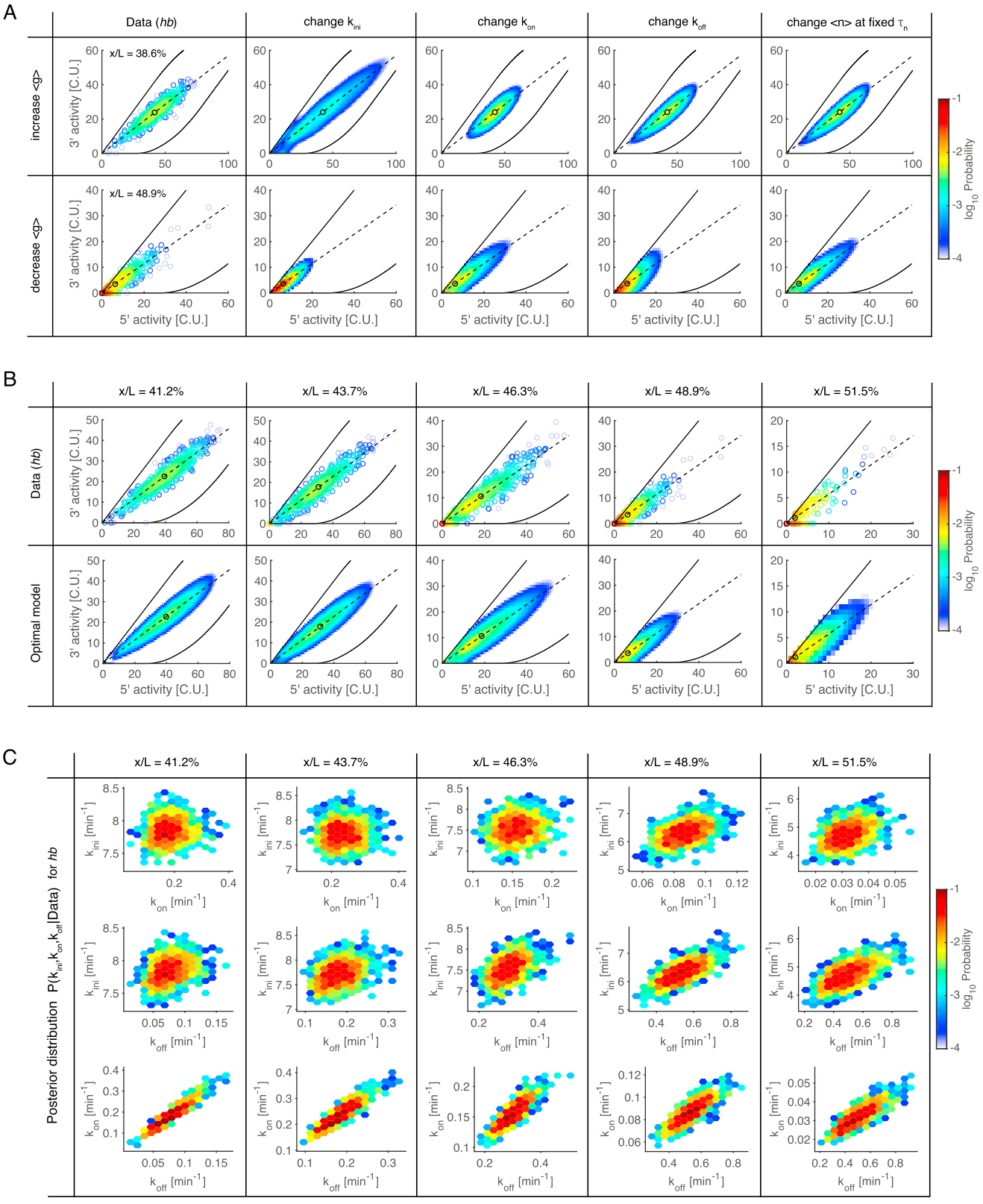

(legend on next page)

Figure S5. Parameter Inference from Dual-Color smFISH Activity Distribution Using the Two-State Model, Related to Figure 4

(A and B) The data correspond to the measured distribution of 3′ versus 5′ activity across AP position for *hb*. Data distributions were constructed based on the 2.5%-AP-bins defined in Figure 4C. Dashed black line represents the expected ratio of 3′ versus 5′ activity ($r = 0.57$ for *hb*); black circle corresponds to the mean of the distribution and lies on the dashed line.

(A) Qualitative change of the distribution predicted by the 2-state model as the parameters vary for AP-bin at $x/L = 38.6\%$ (top row) and at $x/L = 48.9\%$ (bottom row). Changes in the transcriptional parameters k_{ini}, k_{on}, k_{off}, and in $\langle n \rangle$ at fixed τ_n set at the same mean activity $\langle g \rangle$ as in the data leads to qualitatively different distributions. Thus, all information regarding the kinetic parameters is contained in the distribution of 3′ versus 5′ activity, which enables inference of these rates.

(B) Side by side representation of the empirical (data, top row) and modeled (bottom row) distributions with best-fit parameters for different AP bins. The empirical distributions are used as input in our inference framework enabling precise inference of the underlying transcriptional kinetics at each AP position. Of note, the displayed modeled distributions are devoid of measurement noise and represent the theoretical output of the two-state model given the probe-set configuration and the effective elongation time. Thus, the likelihood of the data is essentially the convolution of the activity distribution calculated from the two-state model with the noise measurement distribution. Overall, the best-fit distributions reproduced the data well.

(C) Joint posterior distribution of the parameters given the data in (B) for each AP position. These distributions are generated as the output of our inference framework, namely we sampled the posterior distributions calculated from the likelihood according to Bayes' rule using a Markov chain Monte Carlo (MCMC) algorithm. As the joint posterior distributions are highly peaked in the parameter space, it indicates that the parameters of the model are identifiable for all AP positions. The optimal kinetic rates k_{ini}, k_{on} and k_{off}, which were used to generate the modeled distribution in (B), are estimated from these joint posteriors as the median of the marginal posterior distributions.

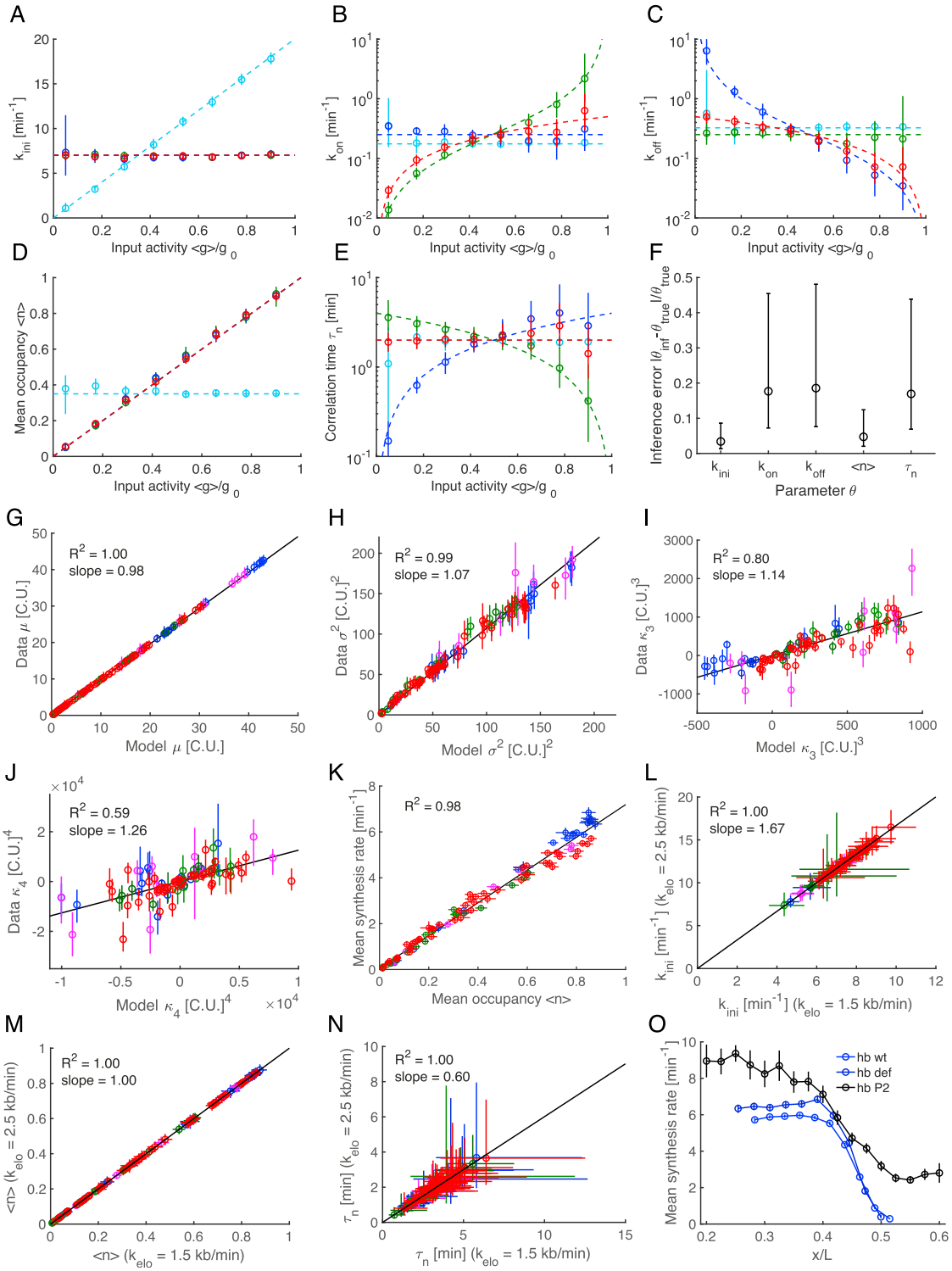

Figure S6. Validation of the Inference Framework for Dual-Color smFISH and Synthesis Rates, Related to Figures 4 and 5

(A–F) We simulated synthetic 3′ and 5′ nuclear activity data based on four gene copies (two alleles with two sister chromatids each) modeled by a two-state model with measurement noise, using the probe configuration for *hb*. To test the performance of our inference, we generated four different datasets by modulating the mean input activity $\langle g \rangle$ in the data through: 1) initiation rate k_{ini} alone (cyan), 2) on-rate k_{on} alone (green), 3) off-rate k_{off} alone (blue) and the mean occupancy $\langle n \rangle$ at constant switching correlation time τ_n (red). The constant g_0 corresponds to the maximal activity for each dataset, defined as $g_0 = \max(k_{ini})\tau_e$, where the maximum is taken over the dataset when k_{ini} varies (cyan) and τ_e is the elongation time. Importantly, the inference of the kinetic parameters was performed for

(legend continued on next page)

each sub-dataset independently (individual circles; 500 nuclei), without assuming any continuity in the dataset. To take into account finite size sampling variation in the data, we inferred parameters on 10 replicates for each synthetic dataset. Thus, the estimated posterior distributions are aggregated over all replicates.
(A–E) Inferred kinetic rates k_{ini} (A), k_{on} (B), and k_{off} (C), mean occupancy $\langle n \rangle = k_{on}/(k_{on}+k_{off})$ (D) and switching correlation time $\tau_n = 1/(k_{on}+k_{off})$ (E) as a function of the mean input activity $\langle g \rangle / g_0$. All quantities are estimated from the sampled joint posterior distribution of the kinetic rates. Colored circles stand for the inferred parameters as a function of input activity, i.e., the median of the marginal posterior distribution. Error bars correspond to the 10^{th} and 90^{th} percentiles of the posterior distribution. The colored dashed lines represent the input (true) parameters used to simulate the data.
(F) Global relative inference error $|\theta_{inf} - \theta_{true}|/\theta_{true}$ calculated for each parameter θ. These errors are estimated over all synthetic datasets and replicates and correspond to the median with error bars given by the 68% confidence intervals. Notably, k_{ini} and $\langle n \rangle$ are easier to infer than the switching rates k_{on} and k_{off} or the correlation time τ_n, which have more subtle effect on the shape of the activity distribution. Still, the inference is able to distinguish between small differences in parameter modulation. Overall, the errors remain small, as the medians of the inference errors never exceed 20% of the true values.
(G–J) Four first cumulants of data (unnormalized, in cytoplasmic units) as a function of the ones predicted by the two state-model with best fitting parameters for multiple gene copies ($N_g = 2, 4$). Each data point corresponds to a single AP-bin. Error bars are the 68% confidence intervals. Overall, the slopes close to one and the large R^2 indicate that the model captures the first four cumulants of data well. Color code as in Figure 1C.
(K) Inferred mean synthesis rate $k_{ini}\langle n \rangle$ as a function of the mean occupancy $\langle n \rangle$ for all genes. Modulation of transcript mean synthesis rate across boundaries is fully determined by the mean occupancy. Color code as in Figure 1C. All error bars correspond to the 10^{th} and 90^{th} percentiles of the posterior distribution.
(L–N) Comparison of the inferred transcriptional parameters k_{ini}, $\langle n \rangle$ and τ_n assuming two different elongation speeds k_{elo} (1.5 kb/min versus 2.5 kb/min). Both k_{ini} and τ_n are rescaled while $\langle n \rangle$ remains the same. Thus, our results are unaffected by the exact value of k_{elo}; it only leads to a rescaling of the inferred parameters that have time units. Color code and error bars as in (K).
(O) Comparison of the estimated mean synthesis rate for a single gene copy of endogenous *hb* (wt and deficient) and the synthetic *hb* P2 reporter live-imaged by Garcia et al. (2013) during interphase 13. The reporter corresponds to a minimal version of the *hb* gene that is driven by the P2 promoter and the P2 (proximal) enhancer alone. The mean synthesis rate of the P2 reporter was obtained by multiplying the estimated effective initiation rate and the fraction of active nuclei divided by two (two sister chromatids per locus), as reported in Garcia et al. (2013). Excluding the posterior region ($x/L > 0.45$), where the reporter shows ectopic expression, the estimated mean synthesis rates only differ by approximately 30 to 50%. This difference, in the case of the reporter, likely stems from both larger live-imaging measurement and calibration errors, and potentially reflects different expression rates between the endogenous gene and the synthetic reporter. Nevertheless, the reported synthesis rates estimated through different models and techniques are consistent. Error bars as in (K) except for the *hb* P2 reporter which are standard errors over multiple embryos.